

A Next-Generation Snow Albedo Parameterization for Climate Modeling using Constrained Machine Learning

A. Charbonneau¹, K. Deck¹, T. Schneider¹

¹California Institute of Technology

Key Points:

- Our data-driven albedo scheme achieves improved and generalizable predictions versus existing models at both fine and coarse scales
- A simple scheme using only standard physical inputs provides competitive output at low computational burden
- The utilized framework offers potential for efficient and scalable physical parameterizations in next-generation modeling regimes

arXiv:2606.05419v1 [physics.app-ph] 3 Jun 2026

Corresponding author: Andrew Charbonneau, acharbon@caltech.edu

Abstract

We demonstrate a data-driven parameterization for snow albedo using a constrained neural differential equation that directly predicts a range of snow albedo tendencies from standard snow and meteorological inputs. After training with multi-year in-situ and satellite observations from a wide variety of locations, the scheme effectively reproduces daily albedo evolution across diverse climate zones, with median error under 7.5% (RMSE \approx 0.05), a 10-30% improvement over established models. Furthermore, the model generalizes to sites not seen during training and scales from coarser grids to point locations. The scheme can easily incorporate new features as observational networks expand, offering an adaptive and computationally lightweight framework for next-generation land and climate models.

Plain Language Summary

Snow reflects sunlight back to space, and small changes in its reflectivity (albedo) can influence our climate. Accurately modeling how snow albedo changes over time remains a challenge in climate models. We develop a data-driven approach that learns the rate of change of albedo using commonly available weather and snow measurements, instead of variables that would be unavailable or more uncertain within a climate model. The model is trained using several years of satellite observations from a wide range of environments. Our model reproduces daily changes in snow albedo across many locations with lower error than widely-used alternatives, performing well for both ground measurements and satellite-scale data. Our approach can easily incorporate new observations and is computationally inexpensive, providing a flexible means for aiding next-generation earth science models and beyond.

1 Introduction

Seasonal snowpacks play a crucial role in the cryosphere, influencing climate at small and large scales. They constitute an integrated response to a region’s weather, covering nearly half the Northern Hemisphere land surface in winter while also ranking among the fastest-changing land covers by season (Dong et al., 2014; A. G. Klein & Stroeve, 2002; Hall & Riggs, 2007). They play a significant role in terrestrial energy and water fluxes, with consequences for ecosystem and economic functions such as water supply, agriculture, supply chains, tourism, and environmental hazards (Lee et al., 2023; Hao et al., 2023; Huang et al., 2022). However, snowpacks are sensitive to changing climates, and historical norms of accumulation and melt no longer reliably capture present-day patterns and timing (Aguirre et al., 2023; Rittger et al., 2020). Snow dynamics remain one of the most challenging aspects to represent in simulations of the water cycle (Pirazzini et al., 2018), emphasizing the need for improved snow models that can adapt and generalize to a range of possible futures at seasonal and multidecadal timescales.

Within snow models, one of the most critical parameters affecting the climate system is the snowpack albedo (α), the ratio of reflected to incident shortwave radiation from the snow surface. Broadband snow albedo integrates wavelength-dependent snow albedo over the spectrum of incoming radiation (Bair et al., 2019):

$$\alpha = \frac{\int_{\lambda_1}^{\lambda_2} \alpha(\lambda) S(\lambda) d\lambda}{\int_{\lambda_1}^{\lambda_2} S(\lambda) d\lambda} \quad (1)$$

where $\alpha(\lambda)$ is the snow’s spectrally-resolved albedo, $S(\lambda)$ is the solar spectral irradiance at the snow surface, and $\lambda_1 = 250$ nm and $\lambda_2 = 4000$ nm are conventional cutoffs for the solar shortwave spectrum. Snow exhibits some of the highest natural albedos on Earth (0.7–0.9), making snow albedo and subsequent energy fluxes uniquely sensitive to per-

turbations or small errors. A small relative reduction in α creates a large relative increase in absorbed shortwave energy ($1 - \alpha$) which accelerates melt and lowers albedo further, amplifying a positive feedback on warming (Bair et al., 2019) and leading to error propagation within global climate models (GCMs) (Qu & Hall, 2006; Thackeray et al., 2018). Through this mechanism, snow albedo exerts a strong control on the surface energy balance and overlying air circulation, and thus regional climate patterns and precipitation (Hall & Riggs, 2007; Malik et al., 2014; Cordero et al., 2022; Kouki et al., 2022; Diro & Sushama, 2018). This influence propagates to global circulation, affecting processes such as ENSO, monsoons, and poleward retreat (Z. Wang et al., 2012), underscoring the need for accurate representation.

Reducing errors in snow albedo is difficult given its variability and multiscale drivers. Snow albedo is governed by a suite of physical processes, including the shape, size, scattering properties, and evolution of snow grains, the concentrations of light-absorbing particles (LAPs) or impurities such as dust and black carbon, snowpack layering and density, atmospheric state, precipitation history, and solar zenith angle (see Warren, 1982; Zhang & Ohata, 2003). However, snow albedo also varies strongly across short spatial and temporal scales due to topography and microclimate (Molotch & Bales, 2006; Williamson et al., 2016), and modification by LAPs often reflects both local and remote sources, decoupling changes from solely local snowpack processes (Bair et al., 2019). Representing the complex interplay of these processes across scales within physical models demands input availability and process fidelity beyond what is contemporarily available at climate scales, leaving even complex schemes uncertain (Gardner & Sharp, 2010; Damiani et al., 2025). Simpler empirical or prescribed formulations to approximate mean behaviors can be useful in mapping local geographic inputs to expected long-term trends, but the assumptions for such schemes rarely generalize beyond their calibration regime. With expanding multi-scale observations spanning diverse climates, a new alternative has become possible: to infer relationships directly from available data, within physical guardrails but without presupposing their functional form. Such a framework to represent physically consistent mappings from local snowpack, climate, and environmental properties to distributions of albedo behavior must capture the integrated effects of the snow and atmosphere while preserving generalizability to diverse climates and changing environments.

Most prevalent snow albedo models are built upon two formative ideas from the 1950s. The first was the application of basic scattering theory to model snow albedo analytically (Dunkle & Bevans, 1956), with later extensions (Wiscombe & Warren, 1980) to incorporate multiple scattering, solar zenith angle, LAPs, and other snowpack properties. The second was the quantification of empirical surface-age and positive-temperature indices in an Army Corps of Engineers report (ACE, 1956) to estimate snow albedo decay. These ideas established the spectrum of theoretical versus empirical approaches to albedo modeling that are still in use today.

Results of these studies are mixed, with complexity showing limited influence on overall parameterization skill and no consensus on which approach best suits large-scale modeling (Gardner & Sharp, 2010; Menard et al., 2021; Essery et al., 2013; Krinner et al., 2018; Magnusson et al., 2015). Empirical age-based schemes reproduce mean decay rates but struggle to capture their variability under changing conditions, routinely producing albedo errors of 10–20% and comparable biases outside their calibration domains (Bair et al., 2019; Etchevers et al., 2004; Damiani et al., 2025; Abolafia-Rosenzweig et al., 2022). This spurred development of detailed process models such as SNICAR, TARTES, and SNOWPACK (Flanner et al., 2021; Lehning et al., 2002) to resolve radiative transfer, microstructure, and spectral effects with higher accuracy, though their usage is generally associated with a larger computational cost at regional scales or modern GCM grids (~ 10 – 100 km) (Gardner & Sharp, 2010; Damiani et al., 2025; Essery et al., 2013; Chan, 2022; Gaillard et al., 2025; W. Wang et al., 2020; He et al., 2024). These and intermediate-

complexity models are also sensitive to input uncertainties, which are poorly constrained at GCM resolutions (Hao et al., 2023; Bair et al., 2019; Menard et al., 2021; Abolafia-Rosenzweig et al., 2022; Gaillard et al., 2025; Voordendag et al., 2021) and often require site-specific calibration. As a result, they show limited transferability across climates and error ranges at large scale that frequently converge back to those of simpler schemes, or can even be outperformed by the latter under uncertain inputs (Etchevers et al., 2004; Lin et al., 2025; Sarangi et al., 2019; Oaida et al., 2015; Shao et al., 2020; Lawrence et al., 2011).

Therefore, many GCMs continue to rely on combinations of a few simple and older parameterizations for scalability, with wide performance spreads highly sensitive to model choice, calibration sites, and validation approaches, especially during the ablation period (Etchevers et al., 2004; Essery et al., 2013; Magnusson et al., 2015; Günther et al., 2019). Age-based schemes remain common despite evidence that more flexible alternatives are superior (Bair et al., 2019). Snow albedo modeling choices have a larger impact on simulations than those for compaction or other processes, with most impact arising from their aptitude in representing varied albedo decay rates and their resulting influence on snowpack decay, which can vary the snow season length by 25-50+ days (Lee et al., 2023; Z. Wang et al., 2012; Etchevers et al., 2004; Essery et al., 2013; Abolafia-Rosenzweig et al., 2022; Painter et al., 2012; Jensen et al., 2024; Ryken et al., 2020). Meanwhile, increasing GCM resolutions and efforts toward finer ($\sim 1-10$ km) or even sub-km land scales to resolve snow albedo variability (Aguirre et al., 2023; Gaillard et al., 2025; Voordendag et al., 2021; Ye et al., 2023; Ding et al., 2024) will further exacerbate these issues of sensitivity, computational burden, and local errors, highlighting the need for efficient but accurate finer-scale schemes for next-generation GCMs; capable of capturing diverse decay rates (Ye et al., 2023; Clark et al., 2015; Schär et al., 2020; Ban et al., 2021).

Recent computational advances and data volume have inspired new albedo parameterization efforts emphasizing grain size, LAP concentration, and spectral resolution to replicate the success of models such as SNICAR/SNICAR-ADv3 with greater efficiency. Studies such as Bair et al. (2019), Gardner and Sharp (2010), Saito et al. (2019), and Ström et al. (2022) report accurate performance across snow conditions, yet these schemes still require complex inputs and inherit the input sensitivity of their predecessors, limiting their utility in GCMs where necessary inputs are often unavailable (Hao et al., 2023; Gardner & Sharp, 2010; Gaillard et al., 2025; Günther et al., 2019; Ye et al., 2023). Machine learning (ML) alternatives offer potential as they easily represent nonlinear interactions and are more robust to uncertainty and nonstationarity (Damiani et al., 2025; Demil et al., 2025; Fleming et al., 2024), yet efforts specific to snow albedo modeling remain scarce. Many focus on snow coverage to improve data fidelity, or largely post-process input reflectance products or predetermined albedo, lacking the physical basis for incorporation into GCMs where such inputs are unavailable (Ding et al., 2024; Zhao et al., 2025; Chen et al., 2025). These efforts presently find limited transferability beyond calibration sites, with many errors still plateauing near $\sim 10\%$ (Ding et al., 2024; Demil et al., 2025; Kiem et al., 2024), and many ML-based approaches do not inherently respect physical constraints (De Michele et al., 2013; Gao et al., 2021).

This work presents a novel parameterization, which uses the machine learning framework developed in Charbonneau et al. (2025) to predict the time derivative of the snow albedo given environmental features and snow state as input. The predictive model output, which obeys prescribed constraints, is then integrated to obtain the broadband snow albedo. It is able to outperform a suite of established models over a large variety of sites from only a single calibration on coarse-scale data, with results that extend from the coarser scales of present data products to fine-scale point validation without recalibration. We use the U.S. Snow Telemetry (SNOTEL) network to gather site-level snow state data, in combination with the STC/MODSCAG-MODDRFS 500-m albedo product (Rittger et al., 2024) to create coarse-level data, along with established validation site data and

automated weather station data to allow testing over a variety of climates. The approach is also accessible to many computational systems and fast to train and prototype (under one minute for training on a single CPU, and able to process millions of inputs per second). It is adaptable as new variables (e.g., characterizing aerosol deposition) become available, demonstrating versatile capability for advancing climate modeling.

2 Methodology

We utilize the framework introduced in Charbonneau et al. (2025) to construct our parameterization, which enforces prescribed constraints (supplied analytical functions, additional parameterizations, etc.) using fixed layers during both training and operation, enabling constrained learning without penalizing the loss function. This scheme was shown to enable efficient, physically consistent, and generalizable parameterizations from simple predictive structures, applicable to a variety of systems and capable of performing on par with more complex models. We combine remotely sensed data in addition to point observations to support benchmarking across scales and a variety of climates. By prioritizing observational data rather than age-based or assimilated features, we avoid circular bias from reanalysis-driven inputs, break from continued reliance on age indices, and achieve more faithful representations of underlying snow processes for usage within GCMs.

2.1 Model

We model the rate of change in snow albedo with a simple neural network, M driving an ordinary differential equation for the evolution of snow albedo:

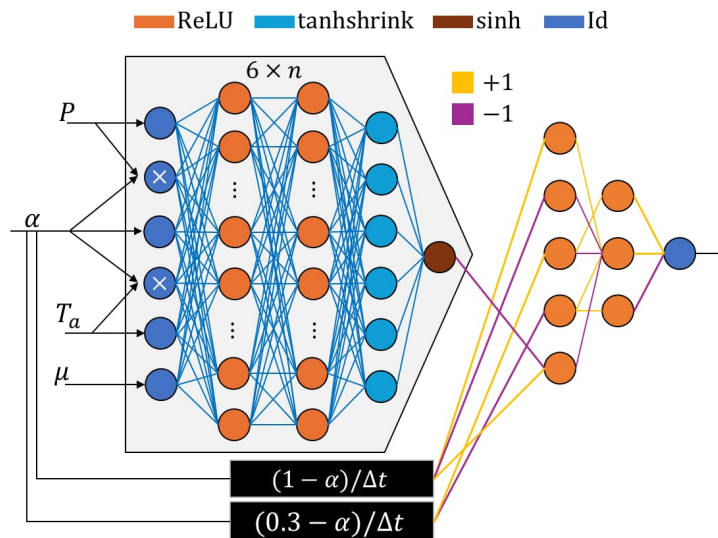


Figure 1. Structure of M . The predictive portion of the parameterization M consists of a simple 3-layer dense neural network with an aggregation to a final output. Nodes are colored by their aggregation function, trainable weights (and a bias term) are shown in blue, and fixed weights (no bias term) are shown in yellow (+1) or purple (-1). One hyperparameter n determines the layer widths. The white “x” indicates multiplication to allow usage of the cross-term inputs αT_a and αP . A threshold constraint layer (see Appendix A in Charbonneau et al., 2025) is included around the predictive component to keep the accumulated albedo between 0.3 and 1 for time-step Δt , even during training.

$$\frac{d\alpha}{dt} = M(\alpha, T_a, P, \mu) \quad (2)$$

where T_a is air temperature ($^{\circ}\text{C}$), P is liquid water-equivalent snowfall rate (m s^{-1}), μ is the cosine of the solar zenith angle (at solar noon for daily data), and α is current albedo (0–1). The network structure is shown in Fig. 1, and constraint functions are picked only to limit the subsequently updated snow albedo value between an applicable range of 0.3 and 1 (Henneman & Stefan, 1999). The constraints are enacted by fixed layers that remain during both training and inference, guaranteeing physically admissible outputs by construction (prohibiting unphysical outputs that would arise from their removal) and improving gradient updates within valid bounds during training. This eliminates the need to add loss function penalties, which can impede optimization of the primary objective (Rahimi et al., 2023), and was shown to protect against overfitting and enable learning of more extrapolative final models, compared to identical models trained without constraints that were only applied afterwards (Charbonneau et al., 2025). Unlike our previous work and other schemes, we did not want to *a priori* restrict albedo increases to occur only under precipitation with the selected constraints, since phenomena like the smoothing of the snow surface during melt or overnight freezing can increase the albedo absent new precipitation. Choosing initial boundaries solely to maintain expected global limits did not presuppose any assumptions about albedo dynamics, and additionally allowed us to explore the extent of the model to learn physically consistent relationships absent additional structure. This prognostic form mirrors the differential equations used for other GCM variables, aiding integration, and reflects findings that prognostic parameterizations are more consistent than other forms (Essery et al., 2013). Learning the rate or change directly via a neural network permits a nonlinear expression of a diverse range of rates from an otherwise simplistic input space, addressing one of the main limitations in previous simple or prognostic schemes (Etchevers et al., 2004; Abolafia-Rosenzweig et al., 2022) and improving representative capacity to observed variability.

We deliberately employ a small black-box neural network (NN) as the internal predictive model within the constraint structure, rather than linear regression, tree-based methods, or other ML approaches. For training volumes available in climate parameterizations and this study, reported tabular-data advantages of tree ensembles diminish (Grinsztajn et al., 2022; Gorishniy et al., 2023), while NNs exhibit stronger expressive capacity for the continuous nonlinear interactions governing albedo. While white-box models like single trees are interpretable, ensemble methods lose most structural transparency, offering little practical interpretability over an intentionally compact NN for GCM integration. Explicit cross-terms and ReLU in the first layer reduce the required depth/width to otherwise learn multiplication and enable explicit representation of “controlled” behaviors (e.g., $(\alpha - \alpha_0) * H(P - P_0)$; H is the Heaviside function) with fewer parameters and operations. Unlike trees, inference with a NN is continuous, fully differentiable, more GPU/cache-scalable without conditional branching, and more compatible with Kalman/gradient-based calibration workflows utilized in GCM sub-model tuning. Our framework with NNs was also shown to permit physically generalizable extrapolation beyond the convex hull of the training targets (Charbonneau et al., 2025), whereas tree models cannot, which is important in evolving climate systems where no data is wholly representative. Convolutional or spatiotemporal networks were not pursued, as the governing processes are effectively localized in the selected input features at GCM-relevant scales, and spatial aggregation amplifies missing-data and uncertainty propagation. We emphasize these choices showcase an informed baseline rather than a final architecture, as the framework remains extensible to alternative model classes and other constraint choices.

Since model complexity shows little correlation with model skill, using a simple network aids computational efficiency, robustness to input uncertainty, and protection against overfitting; all necessary for high-resolution GCMs (Essery et al., 2013; Magnusson et al., 2015). Grain size is deliberately excluded — though often improving diagnostic ac-

curacy, it increases sensitivity and couples performance to an uncertain or unavailable input at GCM scales, it is less directly linked to albedo derivatives than variables like temperature or precipitation (Etchevers et al., 2004; Abolafia-Rosenzweig et al., 2022), and measurements transfer poorly across regions, risking bias and reduced generalizability. Using a 1D model over well-characterized local state variables (i.e., not directly ingesting/requiring spatiotemporal information) allows broad applicability over any spatial grid and better representation of inherently universal processes, while the lack of explicit time dependence within the predictive component (only time-step dependence in the constraints) ensures the scheme can be run at any GCM time step without retraining (Charbonneau et al., 2025).

2.2 Data

We combined in-situ observations from the U.S. Snow Telemetry (SNOTEL) network with the remotely sensed STC/MODSCAG-MODDRFS 500-m albedo product (hereafter “SMM”). SNOTEL provides collocated ground measurements of snow and meteorological variables. In recent years, over 20 SNOTEL sites have also begun to collect surface radiation data, enabling direct snow albedo derivation for site-level validation. For earlier periods, snow albedo timeseries were extracted from the corresponding SMM grid point. SMM improves on earlier MODIS-based products through enhanced corrections for clouds, canopy viewing angle, and ground slope, reducing errors by nearly three-fold against widely used products (e.g., MOD10A1), especially in forested regions where most SNOTEL sensors are located. It more accurately represents snow albedo instead of mixed surface albedo as well as snow onset, disappearance, and melt season dynamics down to lower snow cover fractions (Hao et al., 2023; Aguirre et al., 2023; Rittger et al., 2020; Sarangi et al., 2019; Rittger et al., 2013; Stillinger et al., 2023), with typical validation errors of 0.05–0.08 (Dong et al., 2014; Bair et al., 2019; Painter et al., 2009; Williamson et al., 2016; Painter et al., 2012; Hatchett et al., 2023; Palomaki et al., 2025). Usage of SMM has yielded 10–25% gains in hydrological modeling skill, especially during melt season, underscoring its suitability for next-generation models (Fleming et al., 2024). We are additionally not aware of prior studies using the new SNOTEL albedo data for model validation, offering a novel benchmark. To further test generalization and provide comparable benchmarks, we incorporated standard evaluation sites from Col de Porte (Lejeune et al., 2019), K uhntai (Kraj ci et al., 2017), and Mammoth Mountain (Bair et al., 2018), and include additional data from Sodankyl a (Essery et al., 2016), the Upper Rofental (Warscher et al., 2024), the Himalayas (Stigter et al., 2021; Shea et al., 2015), and one site in Chile from the Centro de Estudios Avanzados en Zonas  ridas (CEAZA) meteorological network, to test performance across out-of-sample elevations and climates.

Both SMM and site sensor data have known quality issues. For SMM, accuracy varies by location and with vegetation cover, and it can exhibit geolocation errors of up to one pixel (Rittger et al., 2020; Bair et al., 2019; Demil et al., 2025; Bair et al., 2022). SMM’s underlying calibration data is not inherently representative of all climates (Keuris et al., 2023) and can influence poor distinction between snow types (Hao et al., 2023), which can bias snow cover fractions and subsequently derived albedos (Lee et al., 2023; see Appendix A). Systematic underestimation of snow-covered areas, summertime values, and misrepresentation of shallow snowpacks (<5 cm) suggest non-snow albedo continues to contaminate reported values (Ding et al., 2024; Palomaki et al., 2025; A. Klein, 2003). For SNOTEL and other site sensors, precipitation is often underreported, and sensor records can contain biased or unphysical values (Meyer et al., 2012; Hill et al., 2019; Warscher et al., 2024). Because no universal cleaning methods exist—particularly for the new SNOTEL albedo records—we developed a custom procedure (see Appendix A) to quality-control, de-noise, smooth, and scale albedo timeseries, supplemented with established methods for other variables (Serreze et al., 1999; Yan et al., 2018; Livneh et al., 2014; Atwood et al., 2023). From cleaned records, $d\alpha/dt$ was derived for days with complete data (excluding $\Delta t > 1$), creating a table of input feature values and an associated tar-

get $d\alpha/dt$ that could be shuffled for training. Daily zenith angle cosine was computed with `Insolations.jl` (Contributors, 2020), and snow–rain fractions were derived using the parameterization from (Jennings et al., 2018), shown to be over 85% accurate. Data scaling constants (standard deviation for inputs, absolute maximum for targets) were fixed in the neural model for reproducibility. This yielded roughly 1.6 million site-days with SMM albedo and 15,300 with direct observations.

2.3 Training and Testing

The combination of SNOTEL sites with the SMM values along with the other validation sites provides two albedo spatial scales for model evaluation: point-scale time-series from ground sensors to assess encapsulation of underlying albedo processes, and extracted 500 m grid-point timeseries to gauge representation of coarse-grained dynamics more relevant for climate models and evolving GCM needs. To emphasize generalizability, the model was trained on a small subset of the coarser SMM data, saving the rest for coarse-scale testing. We also used the same resulting calibration to test over out-of-sample ground-level records from varying climate types, forcing a more stringent test of the parameterization’s capacity to extract and learn relationships that should transfer across scales. We used only the daily data from the 40 SNOTEL sites overlapping with our previous study for training, as these were shown to exhibit sufficient diversity in elevation and local climate to enable robust parameterization (see spread in altitude and snowpack types in Fig. 3 from Charbonneau et al., 2025, as well as Fig. S1 in the Supporting Information for all sites in this study). This left 700 unused SNOTEL sites for coarser testing and 31 site-level test locations, providing extensive performance statistics while highlighting the framework’s ability to generalize from a relatively smaller training sample (~ 87000 batched and shuffled site-day samples from SMM). The model was trained with L_2 loss, using $n = 2$ for the width hyperparameter (see Appendix C for hyperparameter selection), creating a total of 331 weights. Training for 100 epochs (100 passes over all training data) with batch sizes of 256 requires <30 s on a single Intel i9 CPU, with a storage footprint under 2 kB. This likewise competes with the usual training time advantage associated with tree ensembles and other non-adjoint machine learning approaches. Training was implemented in Julia’s `Flux` framework (Innes, 2018) using the root-mean-square propagation (RMSProp) optimizer (Hinton et al., 2012). Data sources and variables are summarized in Table 1.

Table 1. Summary of data and variables. This table denotes the names of utilized data sources and their purpose, as well as the variables mentioned throughout the paper. The Days column refers to the number of sensor days with complete records of at least α , P , and T_a . “Water equivalent” is abbreviated as “w. eq”. Bulk Density is represented as a unitless fraction of the density of liquid water, 1000 kg m^3 . Only variables listed in Eq. 2 are used within M . The spread of snowpack types and geographic locations of all sites can be found in Fig. S1 of the Supporting Information.

Source	Data				Variables			
	Sites	Days	Scale	Purpose	Symbol	Units	Name	Description
SNOTEL/SMM Albedo	40	86841	500m	Training	α	None	Snow Albedo	Derived, see Appendix A
SNOTEL/SMM Albedo	700	1527868	500m	Testing	P	ms^{-1}	Snowfall (w.eq.)	Direct or derived (Appendix A)
SNOTEL/SNOTEL Radiation	23	5318	Point	Testing	T_a	$^{\circ}\text{C}$	Air Temp.	Averaged to daily level
Col De Porte, France	1	2340	Point	Testing	μ	None	Zenith Angle	Cosine at solar noon
Kühtai, Austria	1	4532	Point	Testing	z	m	Snow depth	Direct data
Sodankyla, Finland	1	317	Point	Testing	SWE	m	Snow w.eq.	Direct data
Bella Vista, Upper Rofental	1	457	Point	Testing	ρ	None	Bulk Density	Derived as SWE/z
Proviantdepot, Upper Rofental	1	741	Point	Testing	τ	days	Snow Age	See below & Appendix A
Yala Basecamp, Himalayas	1	126	Point	Testing	α_g	None	Ground Albedo	Derived, see Appendix A
El Tapado, Chile (CEAZA Network)	1	268	Point	Testing	DOY	None	Day of Year	Derived from Date
Dozier Snow Study Site (CUES)	1	1490	Point	Testing	Date	Date	Date	Direct data
TOTAL	771	1630298			T_s	$^{\circ}\text{C}$	Surface Temp.	Estimated, $\min(0, T_a)$

Magnusson et al. (2015) notes new parameterizations are often benchmarked without comparison against existing models, limiting assessment of their true value. To ad-

dress this, we compare our parameterization against a comprehensive set of alternatives (Table 2), representative of those used in current GCMs (Lee et al., 2023) or proposed in prior studies. Consistent with Magnusson et al. (2015) and similar efforts, alternative schemes are primarily compared as-published beyond adjusting time-step-dependent parameters to daily resolution, since many have already been tuned for global use. Additional recalibration may reduce absolute errors but rarely alters the rough ranking or performance categories of schemes (Essery et al., 2013), making such adjustments unnecessary. However, since our neural parameterization must be calibrated to be compared, for fair and holistic comparison a supplemental benchmarking was included for all schemes upon recalibrating them to the same data (see the Supplementary Information for equations and parameter values).

The benchmarked schemes fall into diagnostic or prognostic classes, with some incorporating internal snow-age or other “latent-state” formulations which rendered them unable to be trained via regression like the neural scheme (see below). All schemes except ours predict albedo rather than its derivative. This distinction leads to three equations for generating time-stepped outputs, diagnostic (Eq. 3), prognostic-value (Eq. 4), and prognostic-rate (Eq. 5, our neural parameterization):

$$\widehat{\alpha}_i = f(\theta_i) \quad (3)$$

$$\widehat{\alpha}_i = f(\widehat{\alpha}_{i-1}, \theta_i) \quad (4)$$

$$\widehat{\alpha}_{i+K} = \alpha_i + (K\Delta t) M(\widehat{\alpha}_i, P_i, T_{a,i}, \mu_i) \quad (5)$$

where a hat indicates the model prediction (and no hat for the observation) and θ_i indicate the scheme’s (denoted f) relevant set of non-albedo input variables at step i . For the neural scheme, the integer K denotes the step size across sequential days ($K=1$) or “gaps” from missing/cleaned/no-snow periods ($K > 1$). We note that when traversing data gaps via an Euler step with $K > 1$, the resulting albedo could violate the bounds dictated by the predictive model (designed for step-size $K=1$), though such error should be attributed to the time-stepping choice, not the parameterization itself. To mitigate this, following our previous work (Charbonneau et al., 2025), a maximum gap size of $K_{\max} = 5$ days was permitted before timeseries were “reset” to observed values $\widehat{\alpha}_{i+K} = \alpha_{i+K}$ if $K > K_{\max}$, and unphysical albedos from $1 < K < K_{\max}$ traversals were likewise clamped to $[0.3, 1]$ to avoid attributing error from the time-stepping choice to the parameterization for fair evaluation, as such issues would not occur within a global model setting. Other schemes were reset for any gaps, giving them a “best-case” comparison. Latent-state schemes were not resumed upon reaching a gap until receiving at least $Q_0 = 3$ mm of liquid-equivalent new snowfall to reinitialize internal snow “age”/state from an otherwise indeterminate value (unless Q_0 was specified differently in their documentation), consistent with theoretical analysis from Wiscombe and Warren (1980), though age/state dynamics after such initialization were dictated only by the scheme.

2.3.1 Calibration of Existing Schemes

Most schemes with an internal snow age (τ) utilized a simplistic threshold formulation equal to the number of days since the last snowfall event ($P\Delta t > Q_0$), allowing *a priori* external engineering of the τ feature and training of such schemes via regression over the same batches as the neural scheme. However, some latent-state schemes used continuous or adaptive expressions, requiring autoregressive sequence-based training. In such cases, “batches” were constructed from contiguous cleaned data segments of at least four days. To avoid indeterminate initial latent states, new sequences were only started at days with $P\Delta t > Q_0$ liquid-equivalent snowfall. Each sequence was initialized with a new latent state and stepped forward by the parameterization using the appropriate form from Eq. (3-5), scoring sequences by comparing simulated and observed albedos using the L_2 norm. All schemes could be trained on their respective batches with the same L_2 optimization framework. The neural scheme (and others) could also be trained

Table 2. Parameterizations compared in this study. We benchmark the proposed parameterization against an exhaustive (and fundamental, as others are similar to those below) list of other simple forms (no grain size, only available macroscopic state variables) used in past and present GCMs or proposed in literature, noting their original appearance and reference consulted for parameter values. The table denotes each scheme’s symbol for usage throughout the paper, as well as the model type (prognostic-rate, prognostic-value, or diagnostic, as PR, PV, and D, respectively), whether the scheme uses a continually- (C) or threshold- (T) based reset of internal snow age/indices, and whether the scheme was calibrated autoregressively (AR) or via regression (yes[Y]/no[N], see below). Equations are provided in the Supporting Information. Models explicitly found in CMIP6 (Eyring et al., 2016) are denoted with an asterisk. Some other CMIP6 parameterizations are very similar to listed table members (e.g. UTOPIA, BATS, T_a Interpolation), or constant values. Other listed schemes have also been used in non-CMIP6 global or regional modeling.

Name	Symbol	Identifiable Origins	Referenced Paper	Variables	Type	P Reset	AR	Has Been In:
ACE Curve, Polynomial	AC	ACE (1956)	Molotch and Bales (2006)	τ	D	T	N	
Exponential Decay (Snow Age)	ED	Riley et al. (1969)	Kondo and Yamazaki (1990)	τ	D	T	N	US ACE HEC-HMS
Exponential Decay (T_a Index)	ET	Ranzi and Rosso (1991)	Ranzi and Rosso (1991)	P, T_a	D	T	Y	
Logistic/Exponential Decay (T_a Index)	LE	Pike et al. (2024)	Pike et al. (2024)	P, T_a, z	D	T	Y	-
VAS	V A	Malik et al. (2014)	Malik et al. (2014)	P, T_a, z, α_g	D	T	Y	-
Brock 2000	BR	Brock et al. (2000)	Brock et al. (2000)	P, T_a, SWE, α_g	D	T	Y	-
Marshall (“Simple” Depth)	MD	Marshall (1989)	Marshall (1989)	τ, SWE, α_g	D	T	N	-
Oerlemans & Knap	OK	Oerlemans and Knap (1998)	Lin et al. (2021)	τ, z, α_g	D	T	N	Noah
ESCIMO	EC	Rohrer (1991)	Strasser and Marke (2010)	τ, T_a	D	T	N	ESCIMO
Interpolation (T_a)*	IT	Roeckner et al. (1992)	Möders et al. (2007)	T_a	D	T	N	ECHAM, ECMWF, JSBACH3
Interpolation (Density)	ID	Greuell and Konzelmann (1994)	Greuell and Konzelmann (1994)	ρ	D	-	N	SOMARS, RACMO2, CLSM
Noah Exponential	LV	Anderson (1968)	Livneh et al. (2010)	τ, DOY	D	T	N	Noah, DHSVM, VIC
SNOWPACK-like	SP	Lehning et al. (2002)	This	P, T_a, μ, z, ρ	D	-	N	SNOWPACK
Zhongyuan & Ohata Density	ZO	Zhongyuan and Ohata (1989)	Zhang and Ohata (2003)	ρ	D	-	N	-
NASA GISS*	NG	Hansen et al. (1983)	Hansen et al. (1983)	P	D	C	Y	GISS Model II, ORCHIDEE, CLSM
CLASS*	CL	Versgely (1991)	Li et al. (2023)	P, α	PV	C	Y	Noah-MP, ISBA, CLASS
UTOPIA	UT	Versgely (1991), Baker et al. (1990)	Cassardo (2015)	P, α, T_s, μ	PV	C	Y	UTOPIA
HTESSSEL*	HT	Versgely (1991), Baker et al. (1990)	Dutra et al. (2010)	P, α, T_s, μ	PV	C	Y	HTESSSEL/ECMWF
Giddings and La Chapelle	GC	Giddings and LaChapelle (1961)	O’Neill and Gray (1972)	α, P, SWE, T_s	D	-	N	-
JULES*	JL	Essery et al. (2001)	Best et al. (2011)	z, α_g	D	C	Y	JULES
Marks 1988	MS	Marks (1988)	Marks (1988)	P, T_s	D	C	Y	SNOBAL
BATS*	BA	Dickinson et al. (1986)	Abolafia-Rosenzweig et al. (2022)	τ, μ	D	T	Y	SNOBAL
ISBA*	IS	Brun et al. (1992)	Decharme et al. (2016)	P, T_s, μ	D	C	Y	Many (Noah-MP, WRF CoLM...)
Neural Network	NN	Prev. Work (Charbonneau et al., 2025)	This	z, T_s, T_a, P α, P, T_a, μ	PR	-	Y	Crocus, ISBA MAR

in this autoregressive manner if desired, though such training was slower (roughly $5\times$) without necessarily leading to better results compared to regression on single-day inputs and targets, leading to autoregressive training being reserved only for the models labeled “Y” for “AR” in Table 2.

2.4 Statistical Analysis

Evaluation metrics included root-mean-square error (RMSE), root-mean-square percentage error (RMSE%), bias (B), and bias-percentage (B%) between simulated and observed albedo timeseries. Statistical significance of RMSE and RMSE% differences across validation and test sites was assessed using the Wilcoxon signed-rank test (Wilcoxon, 1945) at a $p = 0.05$ significance level, a nonparametric method over matched samples that avoids assumptions of normality or equal variance. The input features of the model exhibit non-negligible correlation, which confounds more traditional interpretability methods like Shapley additive explanations (SHAP) analysis, permutation importance, or local interpretable model-agnostic explanations (LIME) (Molnar, 2025). Therefore, to qualitatively assess physical consistency, we derived a first-order accumulated local effects (ALE) plot of the neural parameterization, which isolates the influence of individual features even under correlated inputs. Additional discussion of ALE construction and interpretation is available in Charbonneau et al. (2025), Apley and Zhu (2020), and Molnar (2025).

3 Results

3.1 Model Benchmarking

The distribution of RMSE% scores from all schemes as-published (various symbols, see Table 2) and our approach (*NN*) over both coarser (500-m scale) and site-level (point observations) data not seen during training are shown in Fig. 2. All generated albedos by our scheme show a correlation against observations of $R^2 = 0.786$ over the coarse data and $R^2 = 0.677$ over the site-level data. The average correlation scores over each testing site can be further compared against other schemes in the modified Taylor Diagrams (Elvidge et al., 2014), which show both standard deviations and correlations of simulations and observations (Fig. 3). Table B1 in Appendix B displays numerical RMSE%, RMSE, B, B%, and Wilcoxon Signed Rank (Wilcoxon, 1945) scores comparing our scheme to other schemes.

Our model exhibits a median snow albedo RMSE of 0.049 (RMSE% of 6.8%) across all coarse sites, increasing by less than 1% (RMSE 0.056) for point observations, and with less than 0.01 bias at both scales, improving over 30% from other schemes and surpassing the routine 10% error found in other studies. The distribution of RMSE% scores of our scheme is narrower than that of other schemes, showing a consistent range of performance, with fewer outliers (Fig. 2). The two halves of the violin plot are relatively symmetric, suggesting good generalizability across different climates (consistency across sites) as well as generalizability across spatial scales (500 m and site-level sites). This is further corroborated by a lack of distinct patterns in performance with regards to location or snowpack type (see Fig. S1 in the Supporting Information), suggesting broad applicability. With only one calibration at coarser scales, our scheme shows an ability to readily compete against other models that are specifically calibrated for global usage across a range of locations and resolutions.

Most other schemes show less of an ability to maintain consistent performance when transferring across spatial scales — while *NN* shows slightly better performance on coarse data than site data, other schemes tend to show slightly better performance on site data, which could be influenced by the calibration data used for these models compared to the explicit calibration to coarse data in our approach. The lack of schemes near the unity

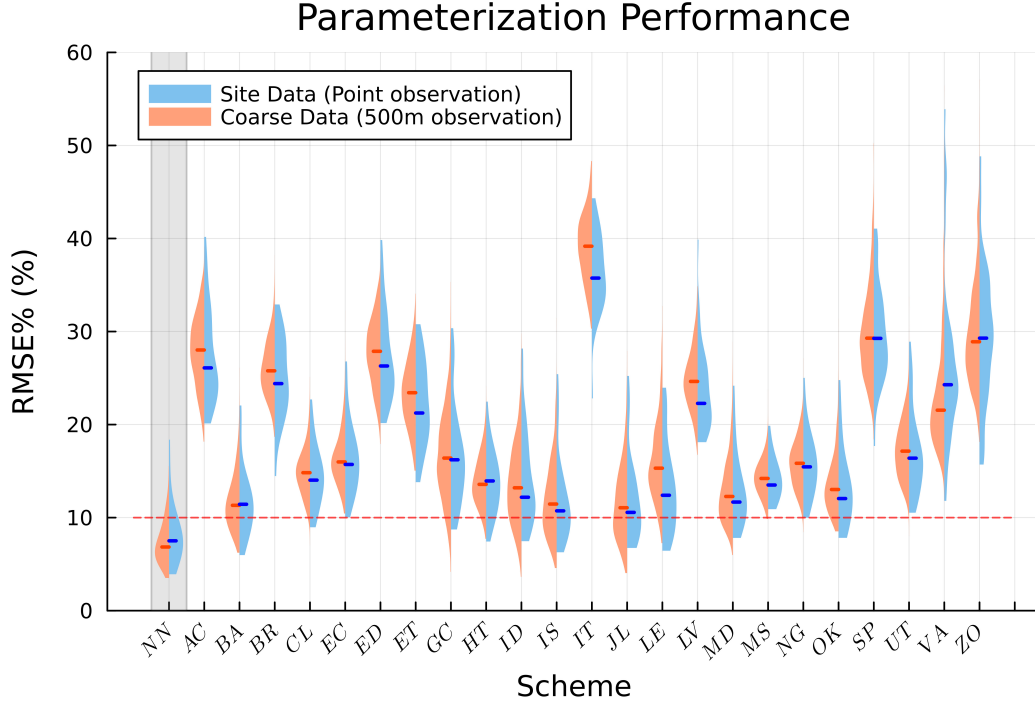


Figure 2. Relative Root Mean Square errors of the new parameterization (*NN*) versus existing parameterizations. This split-violin plot shows the distribution of RMSE% scores for each scheme across all evaluated sites (700 500m scale sites on the left in orange, 31 point observational sites on the right in blue), with the median of each set marked by the horizontal bars. Parameterization symbols match those described in Table 2, and our scheme is highlighted in gray to the left of the other schemes (organized alphabetically; scheme parameters taken as published). Our proposed scheme outperforms all other compared schemes, with the bulk of sites below the marked 10% error threshold (dotted red line) common in snow albedo parameterizations. It also shows good generalizability; with a short tail (a tight spread of scores) and relatively symmetric halves between validation and testing sites (consistent performance across varied out-of-sample regimes). All scores are visible on the plot.

normalized standard deviation contour in Fig. 3 also indicates our model is more capable at replicating the variability of snow albedo observations. Our approach also shows the highest average correlation to observations. All comparisons were significant at the 5% level ($p < 0.05$ for all Wilcoxon tests, with 700 samples for coarse sites and 31 for point-observation sites), detailed in Table B1.

3.2 Model Consistency

Timeseries of our scheme output versus that of well-known top-quintile alternative schemes like BATS (BA), JULES (JL), ISBA (IS), and HTESEL (HT) are given in Fig. 4. Compared to the other schemes, our approach is more able to trace the trends of the albedo within the growth and melt season and match the range of slopes created by the observations across different conditions. By expressing a variety of growth rates, the neural model can better track the seasonal dynamics compared with other models with more rigid evolution structures or a finite set of growth and depletion rates. While this is useful over accumulated seasonal timescales (and thus useful for gauging the accuracy of accumulated energy fluxes within a GCM), we do note this approach does not capture the abrupt increase in albedo due to new snowfall or fast decreases as well as the other schemes, preferring to instead more smoothly climb and fall and transition between dif-

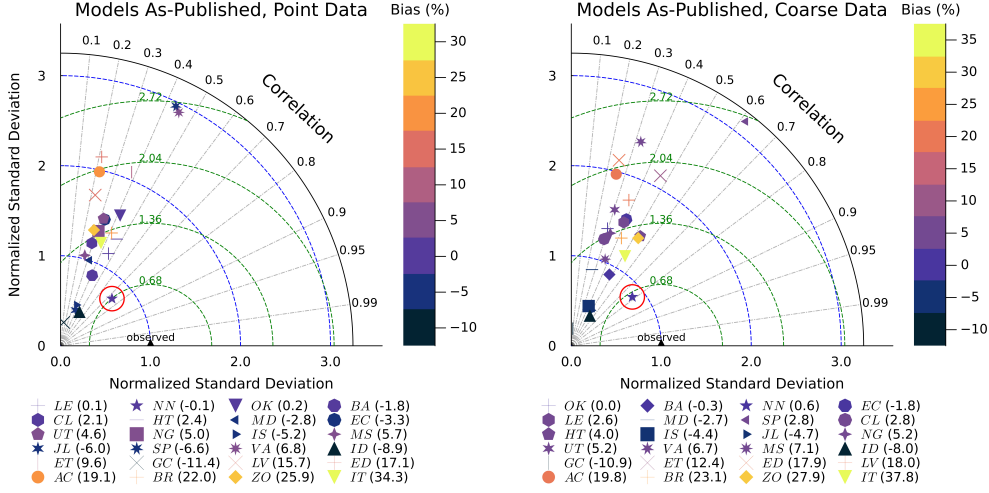


Figure 3. Modified Taylor Diagrams of all schemes over all ground (left) and coarse (right) testing data. The polar coordinates of each scheme mark the standard deviation of timeseries outputs (normalized to that of the observations; the radial coordinate) and the Pearson correlation of timeseries outputs against the observations (the azimuth), averaged over all testing sites. The geometric relationship between standard deviation, correlation, and error means the Euclidean distance from each scheme’s marker to the observations is equal to the centered root-mean-squared (RMS) error against the observations (also equal to the standard deviation in model error), for which contours of centered RMS error are marked in green, contours of normalized standard deviation are marked in blue, and contours of correlation in black. Scheme markers are colored in accordance with their B% score, and the legend is ordered in terms of increasing $|\%B|$, with the value listed next to the symbol. For both types of data, our scheme (circled in red) is best able to replicate the observations with one of the best %B scores.

ferent growth and depletion rates, which is likely influenced by our use of training data at coarser scales, L_2 loss, and data cleaning approaches. At higher temporal resolutions where high-frequency albedo changes can occur from snowfall or intraday zenith angle dependencies, our approach will likely track fluctuations less but track the average well. This emphasis is more conducive to the needs of climate models and long-term studies, where low systematic bias in trends and integrated fluxes is critical over sub-weekly variation or transient fluctuations (National Research Council, 1999; Nguyen et al., 2016).

An Accumulated Local Effects (ALE) plot of our scheme is shown in Fig. 5 below. The ALE plot displays the centered changes in model output (the change in output da/dt compared to the average output da/dt), accumulated over sequential bins of feature values. The accumulation of centered changes instead of displaying averaged outputs over data subsets isolates the model changes independent of feature correlations, allowing interpretation of curve shape (but less so scale) to gauge physical consistency.

The mean prediction of our model over all data is $da/dt \approx 0$, meaning the average changes in model output by feature value align well with physical expectations. Albedo tends to decrease unless there is a minimal amount of snowfall (~ 5 mm liquid-equivalent, see Fig. 5), which then increases but levels off as the amount of snowfall increases after a certain threshold. Similarly, the model begins to tend towards predicting decreases in albedo as temperatures approach and increase past the melting temperature, with a slower rate of change in output near colder temperatures where less melting would occur. While intraday albedo changes decrease and then increase as the sun enters and exits at low zenith angles, the daily albedo trained here uses the zenith angle cosine at lo-

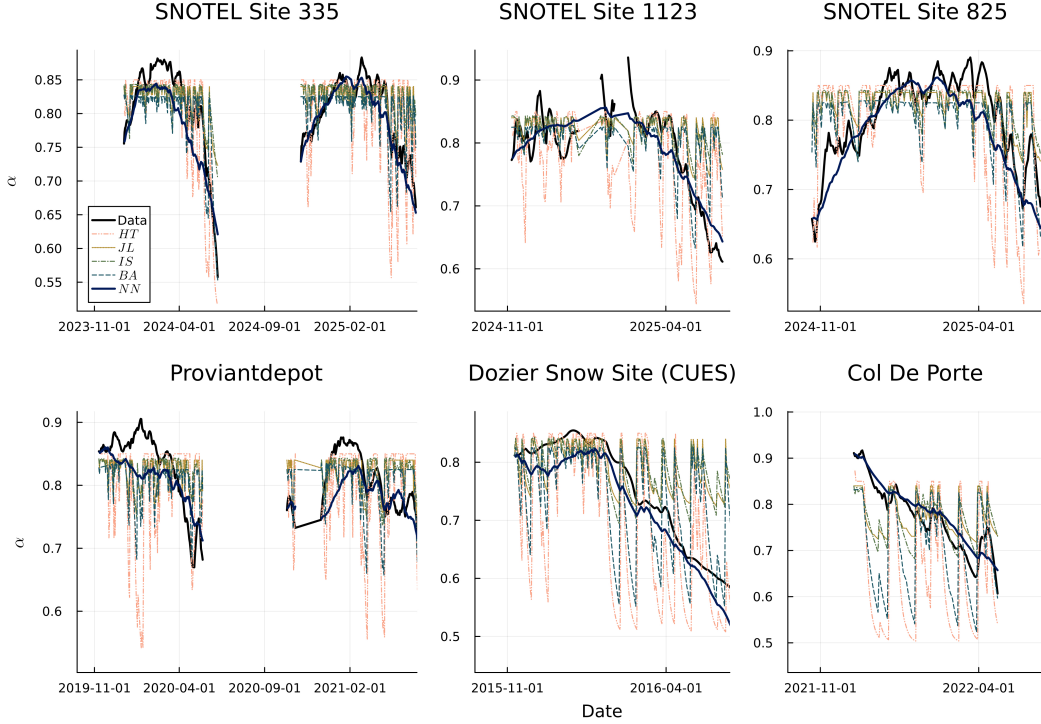


Figure 4. Timeseries of albedo generated by various schemes. This figure details generated timeseries over a selection of site-level testing sites compared to the processed timeseries data, using symbols provided in Table 2. While other schemes show a better capability at creating fast fluctuations or jumps from snowfall, our scheme shows a better ability to follow the overall trend of the albedo throughout the snow season. The shown years were selected to highlight the difference between the trend-tracking behavior of our model vs the fluctuations of other parameterizations.

ALE of Predictors

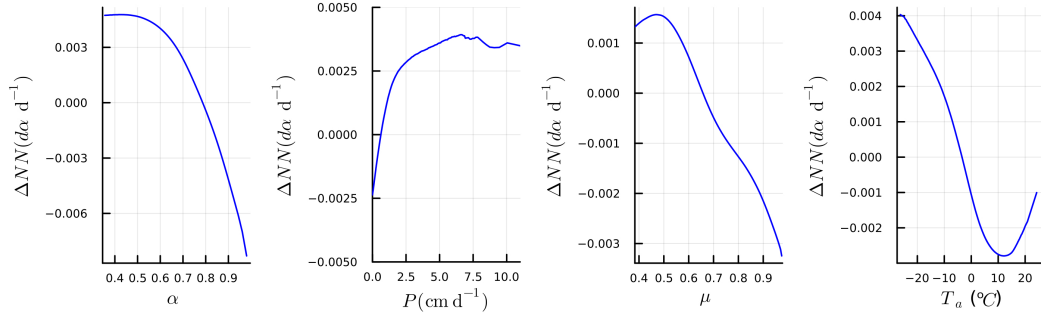


Figure 5. ALE Plot for features of *NN*. The horizontal axes give the range of each of the four input variables (present albedo α , water-equivalent snowfall P , cosine of solar noon zenith angle μ , and air temperature T_a) while the vertical axes show the average change in the scheme relative to the average prediction of albedo change per day (which is $d\alpha/dt \approx 0$). Curves are binned so that each bin has at least 50 samples to average. The rough patch for P after $\sim 5.5 \text{ cm d}^{-1}$ is an artifact of very limited sample sizes in this range, towards the extremes of the available data.

cal noon, which increases during warmer seasons. The plot thus shows the tendency for albedo to decrease during warmer days of the year, again aligning with physical expect-

tations. However, data limitations can influence these results — the concavity at higher T_a could indicate the slowing rate of albedo decrease as albedo approaches its minimal values due to low/no snowpack at the temperature ranges shown, or could alternatively be influenced by the number of samples in the bins at the extreme ranges of the data (there are orders of magnitude less samples after $T_a > 15$ °C or after $P > 6$ cm/day compared to elsewhere along the curve, so statistics can become slightly skewed or the curve become less smooth compared to other feature ranges).

3.3 Calibrated Results

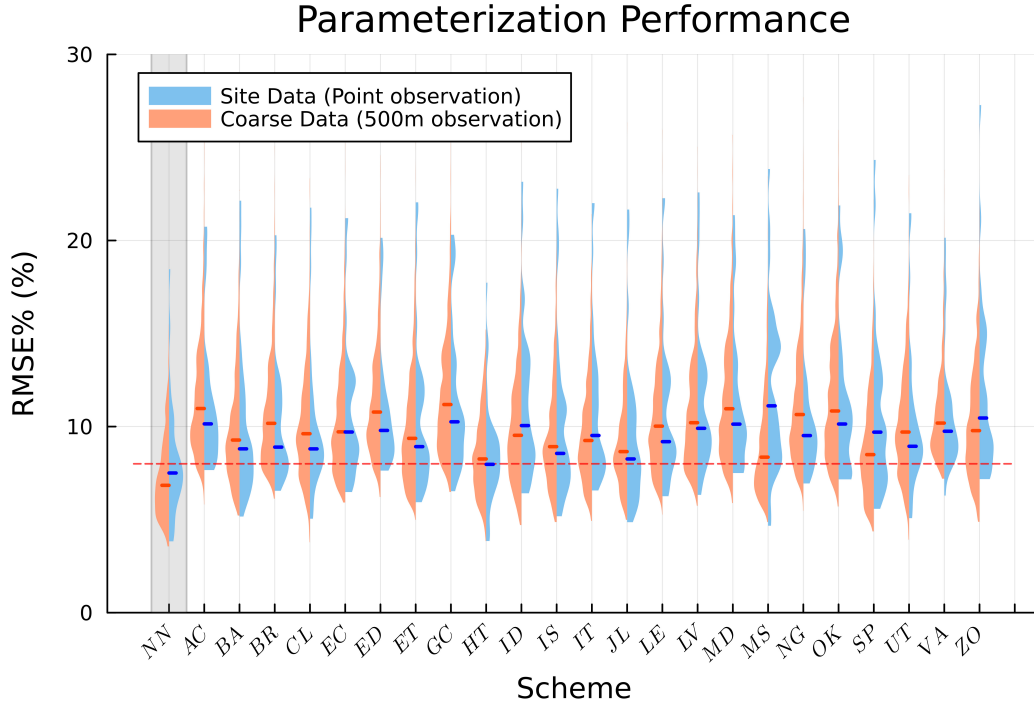


Figure 6. RMSE% scores of all calibrated parameterizations. Format follows that seen in Fig. 2, though this time the red dotted line is placed at an RMSE% of 8% instead of 10% to help better distinguish scheme performance. Our scheme remains clearly separated from other schemes.

A “best-case” ancillary consideration for holistic comparison against our scheme was also examined, by additionally calibrating all other schemes (already designed for global usage) directly to the data to examine the best performance their functional form could achieve (see Overview in the Supporting Information). Calibrating specifically to the same data did not change the overall conclusions and rough scheme ranking, in alignment with findings from Magnusson et al. (2015) and Essery et al. (2013). Many other schemes still show a large number of sites with errors in the 10-20% range after calibration (see Fig. 6), while the bulk of sites at both scales by our model are in the < 10% error range. Even after calibrating the other schemes (maintaining our scheme’s original calibration), our model exhibited significant improvement in RMSE and RMSE% at the 5% level for both coarse and point resolution, except for one insignificant RMSE% score ($p \approx 0.21$) yet a near-significant improvement in the corresponding RMSE score ($p = 0.0695$) against the HTESSEL scheme (HT), for only the point-level data – our model still showed significant improvement over HTESSEL at the coarse level. Despite this, our scheme still showed roughly 0.5 RMSE% (RMSE 0.007) better performance over point-level sites than HTESSEL, and reduced bias by nearly an order of magnitude (see

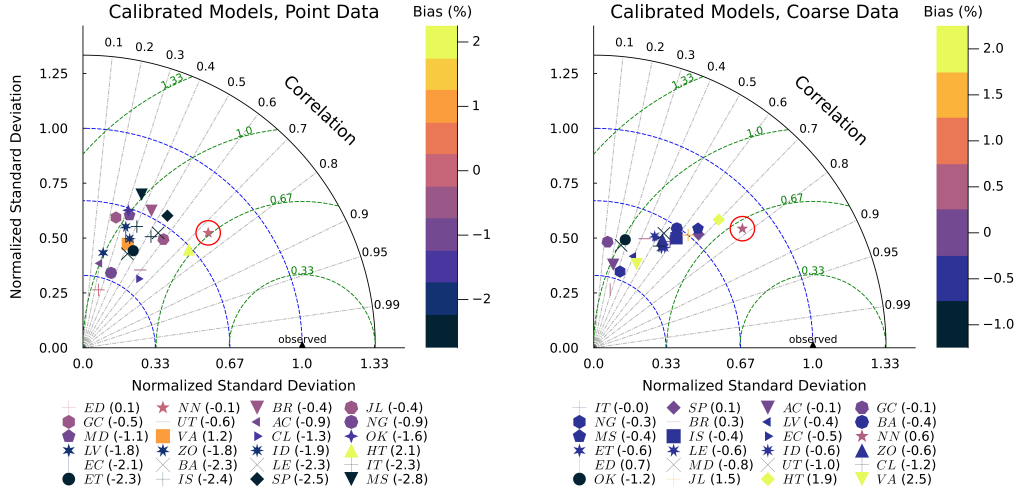


Figure 7. Modified Taylor Diagrams of Calibrated parameterizations. Format follows that seen in Fig. 3. Our model still exhibits the highest average correlation and is the closest to the observed values, though the spread is unsurprisingly tighter than in the uncalibrated case. Our scheme also shows a stronger ability than the other models to match the observational variation in albedo, and is still among the better performers with regards to bias, especially at point scales.

Table B2 in Appendix B). The BATS (BA) and JULES (JL) schemes were still among the better schemes after calibration, though the HTESSSEL (HT) scheme increased in competitive ranking. That our model and other prognostic schemes are among the top performers corroborates earlier findings from Essery et al. (2013), implying prognostic schemes fare better than diagnostic schemes. Even after calibration to the same data, most other schemes still exhibit better performance at the site level than the coarse level - this could be due to their tendency to fluctuate more than the NN, impacting their ability to emphasize the lower-frequency trends that dominate at coarse-grained scales. Fig. 7 shows that calibration aided all schemes in reproducing the variability seen in the data, though our proposed scheme continues to be the best at reproducing the observations, having the second lowest mean B% and top quintile of median B% for point observations. All scheme equations and both their published and calibrated parameters are provided in the Supporting Information.

4 Discussion

Our parameterization improves accuracy by 10–30% relative to standard schemes while maintaining generalizability — a single quick calibration transfers across diverse locations and scales, from site-level ground observations to coarser 500 m grid-point data. This consistency suggests the approach is extracting physically meaningful processes from the input environmental and snow state data that can translate across scales. The results mirror our earlier work developing a similar neural model for snow thickness (Charbonneau et al., 2025), reinforcing the promise of the utilized framework for usage in ever-finer-resolution GCMs. Despite its simplicity, the network maintains accuracy across diverse climate types, which is beneficial both for consistency at global scales and accuracy for local applications. This could aid robustness against nonstationarity and long-term forecasts as climate regimes shift over time, compared to other parameterizations more sensitive to their initial calibration regime. The minimal variable set also decouples the output albedo from compounding errors in other simulated or uncertain inputs that are necessary in alternative schemes, further aiding robustness. Performance levels are within

the 0.05-0.08 RMSE ranges of more complex schemes from radiative-transfer theory like SNICAR (Shao et al., 2020) or full physical models such as Crocus (using the IS scheme) (Gaillard et al., 2025; Alexander et al., 2014) when optimized within a simulation. In real simulation contexts, where coarser scales and uncertain inputs degrade accuracy, these advanced models typically exceed 0.1 RMSE (Hao et al., 2023; Lin et al., 2025; Oaida et al., 2015; Painter et al., 2012), whereas our scheme will not require such intermediate modeling inputs.

The model also demonstrates competitive skill within the ML space. To our knowledge, this is the first application of ML specifically for the parameterization of snow albedo from physical inputs, which can be applied within a GCM for future albedo simulation. Previous work like that of Ding et al. (2024) retrieved snow albedo using non-state inputs such as day of year, top-of-atmosphere reflectance values, and satellite band ratios, but also reanalysis-derived albedo, or that of Zhao et al. (2025) which used gradient-boosted trees and other ML models to predict snow surface albedo from satellite surface reflectance values, trained using simulated data from an atmospheric radiative transfer model. Both studies found their designs improved prediction consistency against site-level observations, achieving mean RMSE $\sim 0.055 - 0.075$ (about 7.5-10.3%), over 101 worldwide sites or 26 sites in Greenland. However, by relying on reanalysis or satellite inputs, it cannot forecast albedo forward in time from the present within coupled systems, limiting the approach to post-processing instead of prognostic use. Comparable ML efforts (e.g., Chen et al., 2025; Kiem et al., 2024; J. Jia et al., 2025) and statistical approaches (e.g., Ye et al., 2023; A. Jia, Wang, Liang, Peng, & Yu, 2023) achieve similar accuracy but rely on geographic indices or predictors such as satellite band ratios, which constrain resolution and applicability and reduce physical interpretability. Our smaller, simpler scheme achieves similar results to these state-of-the-art studies and other ML techniques, while trained on only $\sim 5\%$ of available samples and only physical inputs, ensuring interpretability and long-term applicability. Chevrollier et al. (2025) trained a neural network to emulate SNICAR along with a network inversion technique to additionally infer surface properties from input albedo spectra. Their approach achieved substantial speed-up relative to the full radiative transfer model while diagnosing spectrally resolved albedo (212 bands) with albedo errors below 0.01. However, the emulator needed over 5 million training samples to train 12 layers and 266k parameters, orders of magnitude more parameters than entire GCMs; limiting feasibility for online fine-tuning within GCM ensembles. As with the SNICAR model they emulate, their performance depends on precise input availability (snow grain size, liquid water content, pollutant concentrations, or full 212-band spectra for inversion), requirements unlikely to be met in near-term climate modeling. The reported cost of inversion to obtain such surface properties (~ 0.1 s per grid point) likewise severely constrains scalability for global models. In contrast, our standalone albedo dynamics model is nearly 1000x smaller, enabling online tuning and rapid prototyping, and achieves our results with 100x less data, requiring under $2 \mu\text{s}$ per grid point. More notably, it does not inherit the assumptions in an underlying model (e.g., constant snow density and semi-infinite snow depth for the SNICAR emulator), thereby avoiding associated downstream biases.

The model outcomes are constrained by the context, uncertainty, and limitations of the available data. The SNOTEL network and site-level observations capture localized relationships but are noisy, prone to quality issues, and do not represent large-scale heterogeneity, particularly in complex terrain (Meyer et al., 2012; Hill et al., 2019). The STC/MODSCAG-MODDRFS product likewise suffers terrain as well as cloud effects and is less accurate in forests, partly because its reference spectra exclude burned vegetation. This omission is noteworthy as soot- or fire-derived LAPs increasingly drive abrupt albedo darkening in forested regions, where most SNOTEL sensors reside (Jensen et al., 2024). Both data sources are affected by persistent obfuscation from debris, vegetation, or shadows, and lack coverage in extreme snow environments like tundra and taiga biomes, leaving our model’s extension to these domains untested. The utilized SNOTEL sites express

a range of possible LAP environments, but are not wholly encompassing, so it is possible that areas with more extreme sand or soot content could yield biased model estimates. The tradeoff between smoothing noisy timeseries and preserving short-lived fluctuations is difficult to avoid. We favor smoothing in our methodology (see Appendix A for more detail), which provides a stable representation of the trends relevant for climate modeling, though this can blur the true input-output relationships; potentially limiting model extension to sub-daily scale variability without retraining. Separability of learnable albedo responses is also restricted by the chosen inputs, which cannot capture LAP concentrations, wildfires (Hatchett et al., 2023), grain size, snow chemistry (Sarangi et al., 2019), or atmospheric state. Aggregating these influences into one broadband albedo, rather than spectral or direct/diffuse components, compounds this challenge, especially near more extreme $d\alpha/dt$. While additional variables could represent more processes, direct measurement of such effects is rare, uncertain, or infeasible at GCM scales (Günther et al., 2019; Bair et al., 2018; Painter et al., 2016). Our framework, however, can readily adapt if such data becomes available. Our errors are already reaching the uncertainty range of modern data efforts themselves, underscoring the effectiveness of the modeling paradigm but implying further model gains are unlikely without significant advances in observational quality and availability.

The model captures a diverse range of $d\alpha/dt$ well but struggles with sharp increases from new snowfall at the site level. This limitation likely reflects data separability issues for extreme $d\alpha/dt$ from both the input variable choice (the feature values associated with extreme $d\alpha/dt$ are also associated with other non-extreme targets within the spread of data) and the cleaning techniques, as well as the selected L_2 loss, which emphasizes long-term statistics over individual predictions. Prognostic schemes also require an initial albedo value at the onset of a new snowpack, which can vary by environment (Abolafia-Rosenzweig et al., 2022), leading to spin-up effects. However, high-frequency albedo variation at point-scales will be suppressed in the coarse-graining over grid cells within a GCM. While replicating extreme and sub-weekly variability are important for event-level and point-scale studies in the earth sciences, seasonal energy balance and time-integrated radiative effects dominate evolution within an earth system model and long-term simulations, as these govern large-scale feedbacks and equilibrium responses (Qu & Hall, 2006; National Research Council, 1999). This leaves our computationally efficient approach well-suited for GCM integration. A small network structure can approximate a variety of nonlinear functions while maintaining linear computational scalability. This also lowers overfitting risk while evading the rigidity of symbolic functions with even fewer parameters. This contrasts with competing age-based parameterizations, which rely on precise knowledge of snowfall timing that are uncertain at large scales (Bair et al., 2019). The proposed scheme adapts better to inherent uncertainty, enables rapid iteration, and can readily incorporate new inputs, motivating broader adoption as observational capacity expands. We note the physically consistent behavior with precipitation was learned even without choosing boundary functions to explicitly enforce it, illustrating the potential for this approach. Further experimentation with alternative analytical boundaries could also enforce other desirable behaviors or further increase consistency beyond this initial investigation.

The parameterization performs well at point scales and timeseries from 500 m resolution. Still, these resolutions are finer than the resolutions of current GCMs, where even more coarse-graining may introduce additional variability. However, the continuing push for finer-resolution highlights our approach as a candidate for the growing needs of next-generation climate models. Benchmarking accuracy and spatial structure within a full model over contemporaneous spatial grids at global scale or by land type was not assessed here, and is being addressed in an upcoming paper where the prognostic model has been integrated into a new land surface model (Deck et al., 2026). Other additional avenues for research include sub-daily time-step evaluation, validation across global flux tower networks, or adapting the framework for spectrally resolved albedo using alterna-

tive MODIS products (e.g., MCD43D) to compare against more complex parameterizations.

5 Conclusion

By developing a simple prognostic parameterization for snow-albedo change that breaks from a continued reliance on snow-age, we simulated seasonal daily snow albedo with a median relative error of under 7.5% across diverse locations (median RMSE of ~ 0.05 at both coarse and point scales). Training over a wide data set creates more generalizable results. Our performance extends from point-scale to coarse-grained data and multiple climate types; outperforming or matching advanced data products, complex physical models, and contemporary ML approaches using only standard physical inputs at low computational burden. This reinforces the potential of a physics-informed, data-driven framework that preserves physical consistency while offering accuracy, scalability, and adaptability for next-generation Earth system models. The approach can be used within larger models and can accommodate evolving observational availability. Because snow cover at different altitudes and locations samples situations that may arise in a future, warmer climate (where snowlines generally move to higher altitudes and latitudes), the generalizability we demonstrated will likely translate to generalizability to different climate states. This first-time application of physics-based ML for snow albedo modeling shows potential for developing more accurate forecasts and effective mitigation strategies in an evolving climate, and offers a flexible path for integrating ML into physical modeling without compromising interpretability or physical consistency.

Appendix A Data Appendix

A1 Remote Data

Many remotely-sensed snow albedo products exist, with MODIS-derived (~ 500 m, daily) products remaining standard despite the emergence of finer but less frequent (< 250 m) imagery. The STC/MODSCAG-MODDRFS 500-m albedo product (hereafter “SMM”) product (Rittger et al., 2020; Painter et al., 2009, 2012; Rittger et al., 2024; Jensen et al., 2024) applies spectral unmixing of MODIS reflectances against simulated radiative-transfer and observational libraries to isolate snow albedo, outperforming empirical products like MOD10A1 that more readily represent the mixed total land surface albedo (Fleming et al., 2024). SMM has been recommended for next-generation model calibration (Fleming et al., 2024), though many studies still rely on outdated products, impairing parameterization accuracy and performance interpretability (Aguirre et al., 2023). SMM ownership recently transferred to Snow Today via the National Snow and Ice Data Center (NSIDC).

Work continues on improving known limitations in SMM data, including pixel geolocation errors (~ 1 pixel), high solar-zenith-angle albedos, vegetation/cloud/topographic interference, spectral library representativeness, and inherent one-to-many ambiguity in the unmixing algorithm (Hao et al., 2023; Rittger et al., 2020; Bair et al., 2019; Jensen et al., 2024; Demil et al., 2025; Keuris et al., 2023). Sensor drift in the Terra/Aqua MODIS sensors also introduces minor bias (Feng et al., 2024), though effects are minimal among the temporal ranges and quality measures present in SMM and this study. NSIDC recently prioritized SPIReS, a newer unmixing algorithm (Rittger et al., 2023), but we used SMM due to broader validation, minor differences in accuracy (Hao et al., 2023; Stillinger et al., 2023), and better availability during much of this study.

A2 In-Situ Data

In-situ data measure collocated snow and meteorological variables, though coverage and variable selection vary widely, with few stations reporting full GCM-relevant parameters (Raleigh et al., 2015). Example instruments for automated measurements in-

clude ultrasonic depth sensors, snow pillows, and tipping-bucket gauges, which often are noisy, downtime-prone, or yield unphysical values (Hill et al., 2019; Fleming et al., 2023). Some QC standards exist in some networks, such as SNOTEL (e.g., Serreze et al., 1999), though many data streams remain raw.

In prior work establishing our parameterization framework (Charbonneau et al., 2025), established quality control protocols were extended across additional variables and sites. Subsets of these procedures (denoted ‘‘CQC’’ henceforth) were reused/modified in this work for snow albedo and SMM integration. MODIS and SNOTEL products generally agree once snow depth exceeds 5 cm (A. Klein, 2003). While site slope/topography data are more rare, most SNOTEL stations are built on cleared flat ground, reducing the need for additional correction.

A3 Data Cleaning Methods

For each of the 804 SNOTEL sites inside SMM bounds, from Oct 1 2000 to Oct 1 2023, daily `albedo_dirty_terrain_corrected`, `snow_fraction`, and `days_without_observation` fields from the corresponding SMM pixel (and 8 surrounding pixels) were paired with SNOTEL snow depth (z), snow water equivalent (SWE), air temperatures (daily average), and accumulated precipitation (AP). Site-years beginning collection after the start of the water-year (October 1st) or sites having under 60 SWE/precipitation values were excluded. SNOTEL values beyond instrument limits (USDA, 2010) were set to missing, and CQC steps 7–13 were applied. Zenith angle (ZA) at solar noon was calculated using `Insolations.jl` (Contributors, 2020) with UTC offsets derived from the free Time-ZoneDB API (<https://timezonedb.com/api>), and precipitation was split into rain and snow using the bivariate logistics model from (Jennings et al., 2018) (>85% accuracy):

$$f = \frac{1}{1 + e^{\gamma + \beta T_a}} \quad (\text{A1})$$

where $\beta = 1.24^\circ\text{C}^{-1}$ (temperature in Celsius) and $\gamma = -1.54$. SNOTEL sites with radiation data used the same steps from June 1 2023 to June 1 2025, with the additional steps for hourly incoming (SW_{INC}) and outgoing (SW_{OUT}) shortwave radiation instead of the three SMM fields:

1. Set negative radiation values to zero
2. Derive hourly albedo α_i as $SW_{\text{OUT},i} / SW_{\text{INC},i}$
3. Excise all α_i outside [0-1]
4. Excise α_i with timestamp $ZA > 90^\circ$ (using `Insolations.jl`)
5. Aggregate all $\alpha_i \leq 0.4$ to daily level (mean), and estimate α_g as the minimum of 0.1 or the median of all aggregated values having $z = 0$ and $P = 0$
6. Aggregate all $\alpha_i > 0.35$ to daily level (mean) to make α_{snow} timeseries
7. Excise $\alpha_{\text{snow},i}$ where z_i or SWE_i are 0, missing, or $\text{SWE}_i > z_i$
8. Excise $\alpha_{\text{snow},i}$ where $P_i = 0$ but $d\text{SWE}/dt_i > 0$ (avoid $d\alpha/dt$ samples under indeterminate snowfall)
9. Fill holes of 5 days or less in remaining α_{snow} via linear interpolation
10. Exclude sites with < 60 remaining albedo values

For the SMM albedos (0-100), we used the following steps per site:

1. Excise `albedo_dirty_terrain_correctedi` having `days_without_observationi` > 10, according to Rittger et al. (2024)
2. Apply a power mean ($p=3$) over the remaining 3×3 pixels of `albedo_dirty_terrain_corrected` to mitigate geolocation error, extract the most representative ‘‘snowy’’ estimate (mitigate non-snow or erroneous snow-fraction contamination, with a smoother

non-max norm to avoid amplifying high-frequency noise or biasing towards possible cloud albedos, but more inclined to higher values than an arithmetic mean), and create a more complete α_{snow} timeseries estimate. The count and standard deviation of utilized pixels was tracked.

3. Similarly apply a power mean ($p = -3$, now more inclined to lower values) over the same 3×3 pixels of `albedo_dirty_terrain_corrected`, and estimate α_g as the median of all means ≤ 40 where $z_i = \text{SWE}_i = P_i = P_{i-1} = \text{days_without_observation}_i = 0$. Exclude sites lacking any samples for this estimate.
4. Repeat steps 7-10 from above, excising $\alpha_{\text{snow},i} < 35$ as ground-contaminated signal (this choice was corroborated by the standard deviation over utilized 3×3 pixels at such values being < 8 , while snowy pixels exhibited abruptly higher variation)
5. Scale resulting albedo timeseries by 100 (to [0-1])

Finally, all albedos with $z < 5$ cm were excised to avoid small snowpack discrepancies.

A4 Pre-Training Procedures

Remaining series exhibited unrealistic high-frequency oscillations, especially in-situ or during peak season, exceeding expected daily changes (Sarangi et al., 2019; Bair et al., 2018). These could arise from transient shadows or wind-driven debris, local heterogeneity contamination from the above cleaning procedures, or systematic sensor issues requiring further consideration. At both coarse and site scales, persistent non-snow surfaces (rocks, vegetation, shadows, sensor arrays) can also skew true snow fraction even when reported snow cover fraction is 100% at large snowpack, biasing reported albedo downward (Etchevers et al., 2004; Bair et al., 2022). To address these issues, we applied a two-step correction:

A41 Exponential Smoothing

An exponential moving average (EMA) was applied as a low-pass filter to dampen noise, extracting the trends relevant for climate modeling scales:

$$EMA_i = w\alpha_i + (1 - w)EMA_{i-1} \quad (\text{A2})$$

Other smoothing approaches exist (e.g. Ye et al., 2023; Calleja et al., 2019, though we prefer the EMA due to simpler implementation, true low-pass filtering compared to techniques like max-filtering which can amplify noise, and better preservation of precipitation-driven albedo changes via weighting bias to recent samples. This approach will smooth out some more abrupt authentic transitions and influence the smoothness of the learned dynamics, but also aids in filling out the otherwise more discrete space of raw $d\alpha/dt$ targets due to data precision, which can throttle a neural network’s learning ability. We chose $w = 0.33$ for SMM and $w = 0.1$ for noisier in-situ data to balance noise suppression against preserving physically relevant trends. Each time the EMA was restarted due to missing/cleaned values, the first 5 values were discarded for sufficient burn-in.

A42 Rescaling

A maximum-scaling was applied to correct for persistent non-snow contamination. Measured albedo is a mix of background (α_{bg}) and snow signals weighted by snow fraction, f :

$$\alpha_{obs} = (1 - f_{snow})\alpha_{bg} + f_{snow}\alpha_{snow} \quad (\text{A3})$$

If persistent non-snow contamination prevents full snow coverage ($f_{\max} < 1$) even for peak snowpack in a state of maximum possible albedo ($\alpha_{\text{theory,max}}$), the measured maximum albedo ($\alpha_{\text{obs,max}}$) will be reduced:

$$\alpha_{\text{obs,max}} = (1 - f_{\max})\alpha_{bg} + f_{\max}\alpha_{\text{theory,max}} \quad (\text{A4})$$

Suitable choice of $\alpha_{\text{theory,max}}$ and α_{bg} knowledge thus allows estimation of f_{\max} and a scaling transformation to rescale albedos:

$$f_{\max} = \frac{\alpha_{\text{obs,max}} - \alpha_{bg}}{\alpha_{\text{theory,max}} - \alpha_{bg}}, \quad \alpha_i = \frac{\alpha_{\text{obs},i} - \alpha_{bg}(1 - f_{\max})}{f_{\max}} \quad (\text{A5})$$

Although the best $\alpha_{\text{theory,max}}$ (i.e. fresh pure snowfall on large snowpack) choice could fluctuate by site, it should exhibit tight range across climates and be well-represented within multi-year records, enabling estimation of f_{\max} . The top 5% of all in-situ sites' cleaned albedos were collected, using the mean of these values to estimate $\alpha_{\text{theory,max}} = 0.88$, which aligns with theoretical maximums of broadband albedo (Dozier et al., 2009). This rescaling serves to reduce non-snow contamination and potential unmeasured slope effects, and corrects EMA-induced downward bias while also leaving series with $\alpha_{\text{obs,max}} \approx \alpha_{\text{theory,max}}$ largely unchanged. $\alpha_{\text{obs,max}}$ was estimated with the 95th percentile of each site's cleaned and smoothed albedo measurements, removing and interpolating any $\alpha_{\text{snow}} > 1$ after the transformation.

Daily $d\alpha/dt$ was then computed as $\frac{\alpha_{i+1} - \alpha_i}{t_{i+1} - t_i}$, retaining only consecutive days (when $t_{i+1} - t_i = 1$ day). The final training set excluded cases with `snow_fraction` < 0.05 (the mean over the available 3×3 pixels) and $z/\text{SWE} = 1$, though these were kept in test-ing data. Sites offering less than 30 training samples were excluded from the study.

For non-SNOTEL sites (excluding El Tapado and CUES), non-albedo cleaning is described in CQC, and albedo cleaning followed the steps for SNOTEL above. Col de Porte already gives daily albedo, requiring steps 5,7,8,9 only. For CUES, relative humidity was capped at 1, only albedo steps 4,6,8,9 were used, and snowfall was estimated using the Zwart parameterization (Zwart & Fierz, 2007) from positive changes in z , in accordance with a site representative. No ground albedo was determined but $\alpha_{\text{obs,max}}$ was sufficiently high to only apply the EMA. For El Tapado, the following steps were used:

1. Excise negative z , SWE, and AP ; $AP > 1$ m, $T_a > 20^\circ\text{C}$ (sensor noise)
2. Use only 2017 and 2019 water years from availability and quality concerns (per site correspondence)
3. Fill T_a in 2017 via lapse-rate interpolation, in accordance with (Voordendag et al., 2021)
4. Calculate changes in AP , setting values < 0.5 mm or negative to zero, then reconstruct cumulative AP from these differences.
5. Apply all SNOTEL albedo steps and CQC steps 9-13

The feature set was largely driven by near-term availability, computational simplicity, and quality considerations. Although rain can affect albedo (Xie et al., 2024), including P_{rain} had negligible impact on outcome (as in our prior study) and was omitted for computational simplicity. A 12-h offset exists between SNOTEL precipitation (local midnight) and SMM albedo (roughly local noon) measurements, which can blur interpretation of albedo changes and relationship ‘‘separability’’. However, the EMA already coarse-grains changes and additional methods would likely further blur these relationships, so no further adjustment was applied.

Appendix B Performance Statistics

Table B1. Parameterization scores over as-published parameterizations. Performance of the different schemes in this study across both validation and testing sites, denoting models using their labels provided in Table 2 in the main text. Medians are listed, with the mean in parentheses alongside the median, for each of the performance metrics discussed in the text. For both coarse and point-level sites, each scheme also lists the p-value from the Wilcoxon signed-rank tests in this study, comparing each scheme to our proposed scheme (NN). Significant p-values (< 0.05) are listed in bold, as well as the top scheme within each metric, unless no clear winner was determinable. Our scheme is one of the top performers for most metrics, and all statistical tests are significant ($p < 0.05$) comparing the proposed scheme with regards to RMSE and RMSE%. Scores are also similar between coarse and point-level sites for our model, indicating generalizability across spatial scales.

Model	Coarse Testing Data (500 m)			Point Observation)			Site Testing Data			Significance	
	RMSE%	RMSE	Bias%	Bias	RMSE	RMSE%	RMSE	Bias%	Bias	RMSE%	RMSE
<i>NN</i>	6.84 (7.29)	0.0494 (0.0509)	0.46 (0.57)	0.0059 (0.0079)	-	7.51 (8.05)	0.0555 (0.0584)	0.48 (-0.12)	0.0076 (0.0038)	-	-
<i>CL</i>	14.83 (14.9)	0.1095 (0.1089)	2.93 (2.85)	0.0282 (0.0288)	2.87E-116	14.03 (14.43)	0.1050 (0.1061)	2.15 (2.13)	0.0199 (0.0223)	9.31E-10	1.86E-09
<i>OK</i>	13.02 (13.56)	0.0929 (0.0959)	-0.26 (-0.02)	0.0042 (0.0075)	2.88E-116	12.05 (13.3)	0.0872 (0.0945)	-0.46 (0.17)	-0.0004 (0.0067)	6.52E-09	1.3E-8
<i>LIV</i>	24.64 (24.84)	0.1905 (0.1918)	18.27 (18.04)	0.1433 (0.1429)	2.87E-116	22.28 (23.82)	0.1706 (0.1843)	15.06 (15.73)	0.1192 (0.1259)	9.31E-10	9.31E-10
<i>MD</i>	12.27 (12.88)	0.0858 (0.0870)	-2.4 (-2.71)	-0.0109 (-0.0126)	6.06E-116	11.67 (12.91)	0.0855 (0.0887)	-2.11 (-2.84)	-0.0104 (-0.0144)	9.31E-10	1.86E-09
<i>JL</i>	11.06 (11.59)	0.0732 (0.0741)	-4.44 (-4.68)	-0.0276 (-0.0283)	1.3E-111	10.56 (12.15)	0.0723 (0.0800)	-4.77 (-5.99)	-0.0311 (-0.0376)	6.52E-08	4.0E-6
<i>SP</i>	29.29 (29.91)	0.2082 (0.2157)	1.68 (2.97)	0.0046 (0.015)	2.87E-116	29.26 (29.85)	0.2123 (0.2167)	-8.52 (-6.59)	-0.0761 (-0.0509)	9.31E-10	9.31E-10
<i>MS</i>	14.21 (14.25)	0.1097 (0.1093)	7.39 (7.11)	0.0634 (0.0612)	2.87E-116	13.5 (14.11)	0.1041 (0.1081)	6.61 (5.68)	0.0564 (0.0503)	9.31E-10	9.31E-10
<i>UT</i>	17.14 (17.35)	0.1261 (0.1294)	4.95 (5.24)	0.0435 (0.0462)	2.87E-116	16.39 (17.02)	0.1183 (0.1256)	3.28 (4.62)	0.0306 (0.0398)	9.31E-10	9.31E-10
<i>HT</i>	13.57 (13.92)	0.0986 (0.1011)	3.7 (3.96)	0.0309 (0.0339)	2.87E-116	13.94 (13.76)	0.0985 (0.1011)	2.27 (2.39)	0.0205 (0.022)	9.31E-10	2.79E-09
<i>EC</i>	15.98 (16.32)	0.1147 (0.1157)	-1.71 (-1.74)	-0.0105 (-0.0089)	2.87E-116	15.71 (16.4)	0.1154 (0.1163)	-3.2 (-3.33)	-0.0227 (-0.0204)	9.31E-10	1.86E-09
<i>ZO</i>	28.9 (29.91)	0.2267 (0.2329)	27.18 (27.91)	0.2138 (0.2178)	2.87E-116	29.29 (29.45)	0.2348 (0.2301)	26.75 (25.9)	0.2113 (0.2045)	9.31E-10	9.31E-10
<i>IT</i>	39.17 (39.09)	0.3059 (0.3063)	37.87 (37.83)	0.2946 (0.2948)	2.87E-116	35.74 (36.26)	0.2816 (0.2851)	33.02 (34.28)	0.2582 (0.2673)	9.31E-10	9.31E-10
<i>ID</i>	13.2 (13.56)	0.0859 (0.0865)	-7.99 (-8.0)	-0.0545 (-0.0534)	4.46E-115	12.19 (14.22)	0.0874 (0.0939)	-8.33 (-8.87)	-0.06 (-0.0594)	1.86E-09	1.77E-08
<i>BA</i>	11.32 (11.69)	0.0778 (0.0795)	-0.24 (-0.29)	0.0029 (0.0037)	2.87E-116	11.43 (11.72)	0.0813 (0.0810)	-1.42 (-1.77)	-0.0058 (-0.007)	1.3E-8	2.86E-7
<i>VA</i>	21.55 (23.13)	0.1588 (0.1740)	4.46 (6.62)	0.0371 (0.0555)	2.87E-116	24.28 (26.5)	0.1776 (0.1900)	4.1 (6.83)	0.0321 (0.0525)	9.31E-10	9.31E-10
<i>LE</i>	15.31 (16.07)	0.1047 (0.1101)	2.44 (2.62)	0.0228 (0.0245)	2.87E-116	12.4 (13.27)	0.0846 (0.0898)	0.32 (0.06)	0.0073 (0.0054)	6.52E-08	2.36E-7
<i>AC</i>	28.02 (27.89)	0.2192 (0.2175)	20.22 (19.78)	0.1612 (0.1577)	2.87E-116	26.09 (27.44)	0.2040 (0.2124)	17.16 (19.07)	0.1357 (0.1507)	9.31E-10	9.31E-10
<i>GC</i>	16.4 (16.67)	0.1065 (0.1065)	-10.73 (-10.88)	-0.0734 (-0.0737)	3.88E-116	16.22 (16.68)	0.1062 (0.1090)	-10.97 (-11.43)	-0.0746 (-0.0776)	1.86E-09	2.79E-09
<i>NG</i>	15.84 (15.8)	0.1178 (0.1181)	5.31 (5.24)	0.0464 (0.0464)	2.87E-116	15.46 (15.59)	0.1130 (0.1169)	4.25 (4.96)	0.0375 (0.0434)	9.31E-10	9.31E-10
<i>ED</i>	27.88 (27.77)	0.2167 (0.2159)	18.42 (17.93)	0.1464 (0.1433)	2.87E-116	26.3 (27.38)	0.2022 (0.2111)	15.35 (17.08)	0.1201 (0.1353)	9.31E-10	9.31E-10
<i>ET</i>	23.42 (23.43)	0.1722 (0.1748)	12.04 (12.47)	0.0935 (0.0972)	2.87E-116	21.24 (22.2)	0.1625 (0.1656)	7.66 (9.57)	0.0643 (0.0759)	9.31E-10	9.31E-10
<i>BR</i>	25.78 (26.08)	0.2028 (0.2054)	22.91 (23.06)	0.1808 (0.1825)	2.87E-116	24.4 (25.07)	0.1939 (0.1961)	21.86 (21.97)	0.1741 (0.1724)	1.86E-09	9.31E-10
<i>IS</i>	11.46 (11.91)	0.0756 (0.0773)	-4.24 (-4.35)	-0.0255 (-0.0255)	4.02E-113	10.73 (11.99)	0.0751 (0.0796)	-4.38 (-5.24)	-0.028 (-0.0322)	1.57E-07	7.01E-6

Table B2. Parameterization scores over calibrated parameterizations. Labeling and formatting follows that as described in Table B1. In this case, the proposed scheme is still dominant in many metrics. Results of statistical tests are again all significant ($p < 0.05$) with the exceptions of *HT* over point-level data.

Model	Coarse Testing Data (500 m)			Site Testing Data (Point Observation)			Significance		
	RMSE%	RMSE	Bias%	Bias	RMSE	Bias%	RMSE%	RMSE	RMSE%
<i>NN</i>	6.84 (7.29)	0.0494 (0.0509)	0.46 (0.57)	0.0059 (0.0079)	7.51 (8.05)	0.0555 (0.0584)	0.48 (-0.12)	0.0076 (0.0038)	-
<i>CL</i>	9.62 (10.1)	0.0674 (0.0680)	-1.14 (-1.23)	-0.0029 (-0.0024)	8.8 (9.83)	0.0646 (0.0677)	-0.7 (-1.34)	-0.0017 (-0.0031)	3.15E-04
<i>OK</i>	10.84 (11.52)	0.0750 (0.0770)	-0.94 (-1.24)	0.0003 (-0.0005)	10.14 (11.17)	0.0723 (0.0770)	-0.77 (-1.62)	0.001 (-0.0039)	1.93E-07
<i>LV</i>	10.21 (10.85)	0.0720 (0.0737)	-0.28 (-0.41)	0.0045 (0.0049)	9.91 (11.47)	0.0758 (0.0792)	-0.68 (-1.77)	0.0001 (-0.0049)	4.00E-08
<i>MD</i>	10.96 (11.55)	0.0760 (0.0777)	-0.46 (-0.79)	0.0037 (0.0031)	10.13 (11.43)	0.0722 (0.0790)	-0.2 (-1.11)	0.005 (-0.0001)	5.12E-07
<i>JL</i>	8.65 (9.26)	0.0639 (0.0653)	1.65 (1.57)	0.0171 (0.0179)	8.26 (9.43)	0.0639 (0.0670)	-0.11 (-0.44)	0.0064 (0.0032)	1.04E-02
<i>SP</i>	8.49 (9.01)	0.0596 (0.0609)	-0.02 (0.08)	0.0047 (0.0062)	9.7 (10.56)	0.0673 (0.0732)	-1.99 (-2.49)	-0.012 (-0.0122)	1.19E-05
<i>MS</i>	8.36 (9.11)	0.0591 (0.0612)	-0.29 (-0.44)	0.0023 (0.0022)	11.11 (11.89)	0.0815 (0.0831)	-3.22 (-2.77)	-0.0167 (-0.0138)	1.28E-07
<i>UT</i>	9.71 (10.16)	0.0682 (0.0691)	-0.99 (-1.01)	-0.0013 (-0.001)	8.94 (10.11)	0.0635 (0.0707)	0.05 (-0.58)	0.0034 (0.0025)	1.18E-04
<i>HT</i>	8.26 (8.54)	0.0599 (0.0617)	1.63 (1.89)	0.016 (0.0192)	7.97 (8.5)	0.0633 (0.0638)	3.36 (2.06)	0.0283 (0.0209)	1.72E-03
<i>EC</i>	9.72 (10.43)	0.0680 (0.0703)	-0.35 (-0.46)	0.0038 (0.0036)	9.71 (10.9)	0.0692 (0.0750)	-1.18 (-2.14)	-0.0043 (-0.0086)	2.39E-01
<i>ZO</i>	9.78 (10.26)	0.0666 (0.0686)	-0.77 (-0.62)	0.0008 (0.0025)	10.46 (11.7)	0.0762 (0.0810)	-0.73 (-1.79)	-0.0003 (-0.0054)	1.57E-07
<i>IT</i>	9.25 (9.81)	0.0657 (0.0666)	0.03 (-0.01)	0.0058 (0.0066)	9.52 (10.96)	0.0693 (0.0762)	-2.06 (-2.33)	-0.0096 (-0.0102)	4.99E-07
<i>ID</i>	9.53 (9.99)	0.0648 (0.0668)	-0.7 (-0.57)	0.0003 (0.0024)	10.05 (11.26)	0.0734 (0.0783)	-1.12 (-1.93)	-0.0012 (-0.0067)	2.86E-07
<i>BA</i>	9.28 (9.92)	0.0656 (0.0674)	-0.28 (-0.41)	0.0029 (0.0032)	8.8 (9.95)	0.0617 (0.0684)	-1.29 (-2.31)	-0.0041 (-0.011)	1.38E-06
<i>VA</i>	10.19 (10.72)	0.0754 (0.0768)	2.67 (2.47)	0.0276 (0.027)	9.75 (10.83)	0.0725 (0.0782)	1.92 (1.19)	0.0214 (0.0173)	3.15E-04
<i>LE</i>	10.02 (10.62)	0.0693 (0.0714)	-0.47 (-0.57)	0.0028 (0.0028)	9.19 (10.83)	0.0655 (0.0735)	-1.47 (-2.33)	-0.0056 (-0.01)	1.17E-06
<i>AC</i>	10.97 (11.64)	0.0782 (0.0796)	0.2 (-0.12)	0.0093 (0.0081)	10.14 (11.21)	0.0732 (0.0781)	0.13 (-0.88)	0.0081 (0.002)	2.21E-06
<i>GC</i>	11.18 (11.75)	0.0778 (0.0801)	0.01 (-0.13)	0.0091 (0.0086)	10.26 (11.33)	0.0737 (0.0795)	0.54 (-0.48)	0.008 (0.0054)	1.93E-07
<i>NG</i>	10.65 (11.27)	0.0755 (0.0768)	0.09 (-0.27)	0.0084 (0.0067)	9.52 (10.66)	0.0693 (0.0738)	0.29 (-0.89)	0.008 (0.0016)	8.42E-07
<i>ED</i>	10.78 (11.39)	0.0776 (0.0789)	1.03 (0.73)	0.0156 (0.0147)	9.79 (10.92)	0.0722 (0.0771)	1.02 (0.09)	0.0139 (0.0095)	2.99E-06
<i>ET</i>	9.37 (10.0)	0.0648 (0.0669)	-0.46 (-0.55)	0.003 (0.0027)	8.92 (10.5)	0.0639 (0.0716)	-1.55 (-2.34)	-0.0057 (-0.0103)	7.10E-07
<i>BR</i>	10.17 (10.81)	0.0730 (0.0741)	0.58 (0.33)	0.0115 (0.0107)	8.9 (10.27)	0.0662 (0.0727)	0.97 (-0.35)	0.0134 (0.0048)	9.16E-06
<i>IS</i>	8.92 (9.62)	0.0634 (0.0649)	-0.33 (-0.4)	0.0026 (0.0032)	8.56 (10.07)	0.0641 (0.0694)	-1.86 (-2.39)	-0.0077 (-0.0114)	4.00E-06
									2.15E-04
									1.59E-03

Appendix C Hyperparameters

Similar to our previous work (Charbonneau et al., 2025), we made use of a custom loss-function:

$$L = \frac{1}{N_d} \sum_{i=1}^{N_d} w_i |y_i - \hat{y}_i|^{n_1}, \quad w_i = 1 + |y_i|^{n_2}. \quad (\text{C1})$$

where N_d is the number of batched training data, \hat{y}_i and y_i are the (scaled) prediction and target data, and n_1 and n_2 are constant positive numbers. Using $(n_1 = 1, n_2 = 0)$ or $(n_1 = 2, n_2 = 0)$ is equivalent to optimizing the average L_1 or L_2 losses, respectively. This function enables investigation of emphasizing extremes, which can be important in prognostic (accumulated) modeling as undershooting one extreme $d\alpha/dt$ can propagate the offset to future time steps. Optimal hyperparameters and the assessed values are summarized in Table C1, for n_1 , n_2 , and layer width hyperparameter n . Scores for each configuration were evaluated using leave-one-out validation (training on 39 of the 40 sites, tracking the timeseries RMSE% and bias (B) of the remaining site, and averaging over the 40 possible combinations) with a batch size of 256, tracking performance every 10 epochs over 200 epochs. Most timeseries trials performed optimally when training for approximately 100 epochs with the small network, similar to our previous findings.

Table C1. Hyperparameter results. Timeseries RMSE% and B% were used as the primary metrics. $n_1 = 2$ (L_2 -like metric) provided the lowest RMSE% for all choices.

Parameter	Description	Range	Best Value
n	Width of Mixing Layer	2, 3, 4, 5	2
n_1	Power Scaling of Prediction Error	1, 2, 3	2
n_2	Power Scaling of Target Magnitude	0, 0.1, 1, 2	0

The configuration of $n = 2$, $n_1 = 2$, and $n_2 = 0$ showed optimal performance for both timeseries RMSE% and B. As $n_2 = 0$ matches the L_2 loss function, true L_2 was used for final model training. We note $n_2 \neq 0$ and/or $n_1 = 1$ did often exhibit timeseries that better replicated sub-weekly variation, but at the expense of whole-timeseries offsets that skewed overall performance statistics (which would similarly skew the energy balance within a GCM) to favor $n_2 = 0$. As L_2 loss is associated with RMSE, it is less surprising that $n_1 = 2$ exhibited optimal RMSE%, though optimal $n_2 = 0$ differs from our previous study. This optimal configuration is likely influenced by the relative lack of variation in the coarse-scale (and cleaned) albedo data used for training, compared to the testing site-level data with more variation or the site-level snow depth data in our previous work.

Open Research Section

All utilized data are publicly available. The SNOTEL data utilized in this study are available via the National Water and Climate Center. SNOTEL Data reports were generated using the online portal found at <https://www.nrcs.usda.gov/wps/portal/wcc/home/>. Links to raw and processed data for Col De Porte (Lejeune et al., 2019), Kūhtai (Krajčič et al., 2017), Sodankylä (Essery et al., 2016), Yala (Stigter et al., 2021; Shea et al., 2015), and Upper Rofental (Warscher et al., 2024) data can be found in our previous work (Charbonneau et al., 2025). SMM data can be found at the Snow Today website, hosted by the National Snow and Ice Data Center (NSIDC) https://nsidc.org/data/stc_modscgdrf_hist/versions/1 (Rittger et al., 2024). El Tapado raw data was

retrieved from the CEAZA meteorological network data portal at https://www.ceazamet.cl/index.php?e_cod=TPF&pag=mod_estacion, and CUES data can be found for download at <https://snow.ucsb.edu/index.php/level-2-model-ready> (Bair et al., 2018). The `Insolations.jl` package is developed by the Climate Modeling Alliance (CliMA), able to be downloaded at <https://clima.github.io/Insolation.jl/dev/> (Contributors, 2020), while the API for time-zone retrieval can be found at <https://timezonedb.com/api>. As in our previous work, code for scraping and cleaning data, CSVs of data, and tutorials for data retrieval and modifying our (or building custom) constrained neural networks are available at https://clima.github.io/ClimaLand.jl/dev/generated/standalone/Snow/base_tutorial/, to provide quality-controlled datasets for calibration and ML applications. All data cleaning procedures are described above in Appendix A. Time-stepping is described in the main text. Descriptions and equations of the compared models are provided in the Supporting Information.

Conflict of Interest disclosure

The authors declare there are no conflicts of interest for this manuscript.

Acknowledgments

We thank Edward Bair and Annelies Voordendag for their correspondence regarding CUES and El Tapado data, respectively, and for Cristian Nelson for correspondence about El Tapado data. We thank the Col de Porte, Kuitai, Sodankyla, Upper Rofental, CUES, CEAZA, and Yala Basecamp teams for their data.

A. C. was supported by the AI4Science initiative at the California Institute for Technology and a Department of Defense National Defense Science and Engineering Graduate (NDSEG) Fellowship. All authors were generously supported by Schmidt Sciences, L.L.C. and by the Resnick Sustainability Institute.

Author contributions:

Conceptualization: AC
 Methodology: AC, KD, TS
 Investigation: AC
 Visualization: AC
 Supervision: KS, TS
 Writing – original draft: AC
 Writing – review: KD, TS

References

- Abolafia-Rosenzweig, R., He, C., McKenzie Skiles, S., Chen, F., & Gochis, D. (2022, September). Evaluation and optimization of snow albedo scheme in noah-mp land surface model using in situ spectral observations in the colorado rockies. *Journal of Advances in Modeling Earth Systems*, *14*(10). Retrieved from <http://dx.doi.org/10.1029/2022MS003141> doi: 10.1029/2022ms003141
- ACE. (1956). Snow hydrology: Summary report of the snow investigations. published by the north pacific division, corps of engineers, u.s. army, portland, oregon, 1956. 437 pages, 70 pages of plates, maps and figs., 27 cm.*. *Journal of Glaciology*, *3*(22), 148–148. Retrieved from <http://dx.doi.org/10.3189/S0022143000024503> doi: 10.3189/s0022143000024503
- Aguirre, F., Bozkurt, D., Sauter, T., Carrasco, J., Schneider, C., Jaña, R., & Casassa, G. (2023, November). Snow cover reconstruction in the brunswick peninsula, patagonia, derived from a combination of the spectral fusion, mixture analysis, and temporal interpolation of modis data. *Remote Sensing*, *15*(22), 5430. Retrieved from <http://dx.doi.org/10.3390/rs15225430> doi:

- 10.3390/rs15225430
- Alexander, P. M., Tedesco, M., Fettweis, X., van de Wal, R. S. W., Smeets, C. J. P. P., & van den Broeke, M. R. (2014, December). Assessing spatio-temporal variability and trends in modelled and measured greenland ice sheet albedo (2000–2013). *The Cryosphere*, 8(6), 2293–2312. Retrieved from <http://dx.doi.org/10.5194/tc-8-2293-2014> doi: 10.5194/tc-8-2293-2014
- Anderson, E. A. (1968, February). Development and testing of snow pack energy balance equations. *Water Resources Research*, 4(1), 19–37. Retrieved from <http://dx.doi.org/10.1029/WR004i001p00019> doi: 10.1029/wr004i001p00019
- Apley, D. W., & Zhu, J. (2020, June). Visualizing the effects of predictor variables in black box supervised learning models. *Journal of the Royal Statistical Society Series B: Statistical Methodology*, 82(4), 1059–1086. Retrieved from <http://dx.doi.org/10.1111/rssb.12377> doi: 10.1111/rssb.12377
- Atwood, J., Domonkos, B., Hill, K., Brosten, T., DeMarco, T., Hultstrand, M., ... Buckman, A. (2023). Evaluation of ysi temperature correction equations for bias-reducing snotel network temperature data. In *2023 western snow conference*. Retrieved from https://www.nrcs.usda.gov/sites/default/files/2023-05/Final_Temperature_Correction_Study05262023.pdf
- Bair, E. H., Davis, R. E., & Dozier, J. (2018, March). Hourly mass and snow energy balance measurements from mammoth mountain, ca usa, 2011–2017. *Earth System Science Data*, 10(1), 549–563. Retrieved from <http://dx.doi.org/10.5194/essd-10-549-2018> doi: 10.5194/essd-10-549-2018
- Bair, E. H., Dozier, J., Stern, C., LeWinter, A., Rittger, K., Savagian, A., ... Davis, R. E. (2022, May). Divergence of apparent and intrinsic snow albedo over a season at a sub-alpine site with implications for remote sensing. *The Cryosphere*, 16(5), 1765–1778. Retrieved from <http://dx.doi.org/10.5194/tc-16-1765-2022> doi: 10.5194/tc-16-1765-2022
- Bair, E. H., Rittger, K., Skiles, S. M., & Dozier, J. (2019, September). An examination of snow albedo estimates from modis and their impact on snow water equivalent reconstruction. *Water Resources Research*, 55(9), 7826–7842. Retrieved from <http://dx.doi.org/10.1029/2019WR024810> doi: 10.1029/2019wr024810
- Baker, D. G., Ruschy, D. L., & Wall, D. B. (1990, February). The albedo decay of prairie snows. *Journal of Applied Meteorology*, 29(2), 179–187. Retrieved from [http://dx.doi.org/10.1175/1520-0450\(1990\)029<0179:TADOPS>2.0.CO;2](http://dx.doi.org/10.1175/1520-0450(1990)029<0179:TADOPS>2.0.CO;2) doi: 10.1175/1520-0450(1990)029(0179:tadops)2.0.co;2
- Ban, N., Caillaud, C., Coppola, E., Pichelli, E., Sobolowski, S., Adinolfi, M., ... Zander, M. J. (2021, April). The first multi-model ensemble of regional climate simulations at kilometer-scale resolution, part i: evaluation of precipitation. *Climate Dynamics*, 57(1–2), 275–302. Retrieved from <http://dx.doi.org/10.1007/s00382-021-05708-w> doi: 10.1007/s00382-021-05708-w
- Best, M. J., Pryor, M., Clark, D. B., Rooney, G. G., Essery, R. L. H., Ménard, C. B., ... Harding, R. J. (2011, September). The joint uk land environment simulator (jules), model description – part 1: Energy and water fluxes. *Geoscientific Model Development*, 4(3), 677–699. Retrieved from <http://dx.doi.org/10.5194/gmd-4-677-2011> doi: 10.5194/gmd-4-677-2011
- Brock, B. W., Willis, I. C., & Sharp, M. J. (2000). Measurement and parameterization of albedo variations at haut glacier d’arolla, switzerland. *Journal of Glaciology*, 46(155), 675–688. Retrieved from <http://dx.doi.org/10.3189/172756500781832675> doi: 10.3189/172756500781832675
- Brun, E., David, P., Sudul, M., & Brunot, G. (1992). A numerical model to simulate snow-cover stratigraphy for operational avalanche forecasting. *Journal of Glaciology*, 38(128), 13–22. Retrieved from <http://dx.doi.org/10.3189/S0022143000009552> doi: 10.3189/s0022143000009552

- Calleja, J. F., Corbea-Perez, A., Fernandez, S., Recondo, C., Peon, J., & de Pablo, M. A. (2019, August). Snow albedo seasonality and trend from modis sensor and ground data at johnsons glacier, livingston island, maritime antarctica. *Sensors*, *19*(16), 3569. Retrieved from <http://dx.doi.org/10.3390/s19163569> doi: 10.3390/s19163569
- Cassardo, C. (2015). Utopia: The manual of version 2015. *8594*. Retrieved from <https://www.researchgate.net/doi/10.13140/RG.2.2.29664.38404> doi: 10.13140/RG.2.2.29664.38404
- Chan, H. G. (2022). Parameterization of snowpack albedo reduction by light-absorbing impurities. *Geophysical Fluid Dynamics Laboratory (U.S.)*. Retrieved from <https://repository.library.noaa.gov/view/noaa/45392> doi: 10.25923/527J-0A46
- Charbonneau, A., Deck, K., & Schneider, T. (2025, July). A physics-constrained neural differential equation framework for data-driven snowpack simulation. *Artificial Intelligence for the Earth Systems*, *4*(3). Retrieved from <http://dx.doi.org/10.1175/AIES-D-24-0040.1> doi: 10.1175/aies-d-24-0040.1
- Chen, S., Xiao, P., Zhang, X., Pellikka, P., Liu, H., & Liu, Y. (2025, October). Mapping snow-covered forest albedo via hybrid radiative transfer and machine learning across northern hemisphere. *ISPRS Journal of Photogrammetry and Remote Sensing*, *228*, 489–504. Retrieved from <http://dx.doi.org/10.1016/j.isprsjprs.2025.07.033> doi: 10.1016/j.isprsjprs.2025.07.033
- Chevrollier, L.-A., Wehrlé, A., Cook, J. M., Pirk, N., Benning, L. G., Anesio, A. M., & Tranter, M. (2025). Separating the albedo-reducing effect of different light-absorbing particles on snow using deep learning. *The Cryosphere*, *19*(4), 1527–1538. Retrieved from <https://tc.copernicus.org/articles/19/1527/2025/> doi: 10.5194/tc-19-1527-2025
- Clark, M. P., Fan, Y., Lawrence, D. M., Adam, J. C., Bolster, D., Gochis, D. J., ... Zeng, X. (2015, August). Improving the representation of hydrologic processes in earth system models. *Water Resources Research*, *51*(8), 5929–5956. Retrieved from <http://dx.doi.org/10.1002/2015WR017096> doi: 10.1002/2015wr017096
- Contributors, C. (2020). *Insolation.jl*. Retrieved from <https://github.com/CliMA/Insolation.jl> (GitHub repository. Apache-2.0 license.)
- Cordero, R. R., Sepúlveda, E., Feron, S., Wang, C., Damiani, A., Fernandez, F., ... Casassa, G. (2022, March). Black carbon in the southern andean snowpack. *Environmental Research Letters*, *17*(4), 044042. Retrieved from <http://dx.doi.org/10.1088/1748-9326/ac5df0> doi: 10.1088/1748-9326/ac5df0
- Damiani, A., Ishizaki, N. N., Feron, S., & Cordero, R. R. (2025, February). Projecting future snow changes at kilometer scale for adaptation using machine learning and a cmip6 multi-model ensemble. *Science of The Total Environment*, *964*, 178606. Retrieved from <http://dx.doi.org/10.1016/j.scitotenv.2025.178606> doi: 10.1016/j.scitotenv.2025.178606
- Decharme, B., Brun, E., Boone, A., Delire, C., Le Moigne, P., & Morin, S. (2016, April). Impacts of snow and organic soils parameterization on northern eurasian soil temperature profiles simulated by the isba land surface model. *The Cryosphere*, *10*(2), 853–877. Retrieved from <http://dx.doi.org/10.5194/tc-10-853-2016> doi: 10.5194/tc-10-853-2016
- Deck, K., Braghieri, R. K., Renchon, A. A., Sloan, J., Bozzola, G., Speer, E., ... Schneider, T. (2026). Climaland: A land surface model designed to enable data-driven parameterizations. *Journal of Advances in Modeling Earth Systems*, *18*(1), e2025MS005118. Retrieved from <https://agupubs.onlinelibrary.wiley.com/doi/abs/10.1029/2025MS005118> (e2025MS005118 2025MS005118) doi: <https://doi.org/10.1029/2025MS005118>
- De Michele, C., Avanzi, F., Ghezzi, A., & Jommi, C. (2013, March). Investi-

- gating the dynamics of bulk snow density in dry and wet conditions using a one-dimensional model. *The Cryosphere*, 7(2), 433–444. Retrieved from <http://dx.doi.org/10.5194/tc-7-433-2013> doi: 10.5194/tc-7-433-2013
- Demil, G., Haghighi, A. T., Klöve, B., & Oussalah, M. (2025, June). Advances in image-based estimation of snow variable: A systematic literature review on recent studies. *Journal of Hydrology*, 654, 132855. Retrieved from <http://dx.doi.org/10.1016/j.jhydrol.2025.132855> doi: 10.1016/j.jhydrol.2025.132855
- Dickinson, R., Henderson-Sellers, A., Kennedy, P., & Wilson, M. (1986). *Biosphere-atmosphere transfer scheme (bats) for the near community climate model* (Tech. Rep.). NATIONAL CENTER FOR: ATMOSPHERIC RESEARCH. Retrieved from <https://doi.org/10.5065/d6668b58> doi: 10.5065/D6668B58
- Ding, A., Liang, S., Ma, H., He, T., Jia, A., & Wang, Q. (2024, December). Improved estimation of daily blue-sky snow shortwave albedo from modis data and reanalysis information. *Science of Remote Sensing*, 10, 100163. Retrieved from <http://dx.doi.org/10.1016/j.srs.2024.100163> doi: 10.1016/j.srs.2024.100163
- Diro, G. T., & Sushama, L. (2018, August). Snow–precipitation coupling and related atmospheric feedbacks over north america. *Atmospheric Science Letters*, 19(8). Retrieved from <http://dx.doi.org/10.1002/asl.831> doi: 10.1002/asl.831
- Dong, J., Ek, M., Hall, D., Peters-Lidard, C., Cosgrove, B., Miller, J., . . . Xia, Y. (2014, April). Using air temperature to quantitatively predict the modis fractional snow cover retrieval errors over the continental united states. *Journal of Hydrometeorology*, 15(2), 551–562. Retrieved from <http://dx.doi.org/10.1175/JHM-D-13-060.1> doi: 10.1175/jhm-d-13-060.1
- Dozier, J., Green, R. O., Nolin, A. W., & Painter, T. H. (2009, September). Interpretation of snow properties from imaging spectrometry. *Remote Sensing of Environment*, 113, S25–S37. Retrieved from <http://dx.doi.org/10.1016/j.rse.2007.07.029> doi: 10.1016/j.rse.2007.07.029
- Dunkle, R. V., & Bevans, J. T. (1956, April). An approximate analysis of the solar reflectance and transmittance of a snow cover. *Journal of Meteorology*, 13(2), 212–216. Retrieved from [http://dx.doi.org/10.1175/1520-0469\(1956\)013<0212:AAAOTS>2.0.CO;2](http://dx.doi.org/10.1175/1520-0469(1956)013<0212:AAAOTS>2.0.CO;2) doi: 10.1175/1520-0469(1956)013<0212:aaaots>2.0.co;2
- Dutra, E., Balsamo, G., Viterbo, P., Miranda, P. M. A., Beljaars, A., Schär, C., & Elder, K. (2010, August). An improved snow scheme for the ecmwf land surface model: Description and offline validation. *Journal of Hydrometeorology*, 11(4), 899–916. Retrieved from <http://dx.doi.org/10.1175/2010JHM1249.1> doi: 10.1175/2010jhm1249.1
- Elvidge, S., Angling, M. J., & Nava, B. (2014, September). On the use of modified taylor diagrams to compare ionospheric assimilation models. *Radio Science*, 49(9), 737–745. Retrieved from <http://dx.doi.org/10.1002/2014RS005435> doi: 10.1002/2014rs005435
- Essery, R., Best, M., & Cox, P. (2001). *Moses 2.2 technical documentation* (Vol. 30). Hadley Centre for Climate Prediction and Research.
- Essery, R., Kontu, A., Lemmetyinen, J., Dumont, M., & Ménard, C. B. (2016, June). A 7-year dataset for driving and evaluating snow models at an arctic site (sodankylä, finland). *Geoscientific Instrumentation, Methods and Data Systems*, 5(1), 219–227. Retrieved from <http://dx.doi.org/10.5194/gi-5-219-2016> doi: 10.5194/gi-5-219-2016
- Essery, R., Morin, S., Lejeune, Y., & B Ménard, C. (2013, May). A comparison of 1701 snow models using observations from an alpine site. *Advances in Water Resources*, 55, 131–148. Retrieved from <http://dx.doi.org/10.1016/j.advwatres.2012.07.013> doi: 10.1016/j.advwatres.2012.07.013

- Etchevers, P., Martin, E., Brown, R., Fierz, C., Lejeune, Y., Bazile, E., . . . Yang, Z.-L. (2004). Validation of the energy budget of an alpine snowpack simulated by several snow models (snow mip project). *Annals of Glaciology*, *38*, 150–158. Retrieved from <http://dx.doi.org/10.3189/172756404781814825> doi: 10.3189/172756404781814825
- Eyring, V., Bony, S., Meehl, G. A., Senior, C. A., Stevens, B., Stouffer, R. J., & Taylor, K. E. (2016). Overview of the coupled model intercomparison project phase 6 (cmip6) experimental design and organization. *Geoscientific Model Development*, *9*(5), 1937–1958. Retrieved from <https://gmd.copernicus.org/articles/9/1937/2016/> doi: 10.5194/gmd-9-1937-2016
- Feng, S., Wehrlé, A., Cook, J. M., Anesio, A. M., Box, J. E., Benning, L. G., & Tranter, M. (2024, June). The apparent effect of orbital drift on time series of modis mod10a1 albedo on the greenland ice sheet. *Science of Remote Sensing*, *9*, 100116. Retrieved from <http://dx.doi.org/10.1016/j.srs.2023.100116> doi: 10.1016/j.srs.2023.100116
- Flanner, M. G., Arnheim, J. B., Cook, J. M., Dang, C., He, C., Huang, X., . . . Zender, C. S. (2021, December). Snicar-adv3: a community tool for modeling spectral snow albedo. *Geoscientific Model Development*, *14*(12), 7673–7704. Retrieved from <http://dx.doi.org/10.5194/gmd-14-7673-2021> doi: 10.5194/gmd-14-7673-2021
- Fleming, S. W., Rittger, K., Oaida Tagliatalata, C. M., & Graczyk, I. (2024, April). Leveraging next-generation satellite remote sensing-based snow data to improve seasonal water supply predictions in a practical machine learning-driven river forecast system. *Water Resources Research*, *60*(4). Retrieved from <http://dx.doi.org/10.1029/2023WR035785> doi: 10.1029/2023wr035785
- Fleming, S. W., Zukiewicz, L., Strobel, M. L., Hofman, H., & Goodbody, A. G. (2023, February). Snotel, the soil climate analysis network, and water supply forecasting at the natural resources conservation service: Past, present, and future. *JAWRA Journal of the American Water Resources Association*, *59*(4), 585–599. Retrieved from <http://dx.doi.org/10.1111/1752-1688.13104> doi: 10.1111/1752-1688.13104
- Gaillard, M., Vionnet, V., Lafaysse, M., Dumont, M., & Ginoux, P. (2025, February). Improving large-scale snow albedo modeling using a climatology of light-absorbing particle deposition. *The Cryosphere*, *19*(2), 769–792. Retrieved from <http://dx.doi.org/10.5194/tc-19-769-2025> doi: 10.5194/tc-19-769-2025
- Gao, L., Zhang, L., Shen, Y., Zhang, Y., Ai, M., & Zhang, W. (2021, September). Modeling snow depth and snow water equivalent distribution and variation characteristics in the irtys river basin, china. *Applied Sciences*, *11*(18), 8365. Retrieved from <http://dx.doi.org/10.3390/app11188365> doi: 10.3390/app11188365
- Gardner, A. S., & Sharp, M. J. (2010, March). A review of snow and ice albedo and the development of a new physically based broadband albedo parameterization. *Journal of Geophysical Research: Earth Surface*, *115*(F1). Retrieved from <http://dx.doi.org/10.1029/2009JF001444> doi: 10.1029/2009jf001444
- Giddings, J. C., & LaChapelle, E. (1961, January). Diffusion theory applied to radiant energy distribution and albedo of snow. *Journal of Geophysical Research*, *66*(1), 181–189. Retrieved from <http://dx.doi.org/10.1029/JZ066i001p00181> doi: 10.1029/jz066i001p00181
- Gorishniy, Y., Rubachev, I., Khrulkov, V., & Babenko, A. (2023). *Revisiting deep learning models for tabular data*. Retrieved from <https://arxiv.org/abs/2106.11959>
- Greuell, W., & Konzmann, T. (1994, January). Numerical modelling of the energy balance and the englacial temperature of the greenland ice sheet. calculations for the eth-camp location (west greenland, 1155 m a.s.l.). *Global and Planetary Change*, *9*(1–2), 91–114. Retrieved from <http://dx.doi.org/10.1016/>

- 0921-8181(94)90010-8 doi: 10.1016/0921-8181(94)90010-8
- Grinsztajn, L., Oyallon, E., & Varoquaux, G. (2022). *Why do tree-based models still outperform deep learning on tabular data?* Retrieved from <https://arxiv.org/abs/2207.08815>
- Günther, D., Marke, T., Essery, R., & Strasser, U. (2019, April). Uncertainties in snowpack simulations—assessing the impact of model structure, parameter choice, and forcing data error on point-scale energy balance snow model performance. *Water Resources Research*, *55*(4), 2779–2800. Retrieved from <http://dx.doi.org/10.1029/2018WR023403> doi: 10.1029/2018wr023403
- Hall, D. K., & Riggs, G. A. (2007, May). Accuracy assessment of the modis snow products. *Hydrological Processes*, *21*(12), 1534–1547. Retrieved from <http://dx.doi.org/10.1002/hyp.6715> doi: 10.1002/hyp.6715
- Hansen, J., Russell, G., Rind, D., Stone, P., Lacis, A., Lebedeff, S., . . . Travis, L. (1983, April). Efficient three-dimensional global models for climate studies: Models i and ii. *Monthly Weather Review*, *111*(4), 609–662. Retrieved from [http://dx.doi.org/10.1175/1520-0493\(1983\)111<0609:ETDGMF>2.0.CO;2](http://dx.doi.org/10.1175/1520-0493(1983)111<0609:ETDGMF>2.0.CO;2) doi: 10.1175/1520-0493(1983)111(0609:etdgmf)2.0.co;2
- Hao, D., Bisht, G., Rittger, K., Stillinger, T., Bair, E., Gu, Y., & Leung, L. R. (2023, February). Evaluation of e3sm land model snow simulations over the western united states. *The Cryosphere*, *17*(2), 673–697. Retrieved from <http://dx.doi.org/10.5194/tc-17-673-2023> doi: 10.5194/tc-17-673-2023
- Hatchett, B. J., Koshkin, A. L., Guirguis, K., Rittger, K., Nolin, A. W., Heggli, A., . . . Haleakala, K. (2023, February). Midwinter dry spells amplify post-fire snowpack decline. *Geophysical Research Letters*, *50*(3). Retrieved from <http://dx.doi.org/10.1029/2022GL101235> doi: 10.1029/2022gl101235
- He, C., Flanner, M., Lawrence, D. M., & Gu, Y. (2024, February). New features and enhancements in community land model (clm5) snow albedo modeling: Description, sensitivity, and evaluation. *Journal of Advances in Modeling Earth Systems*, *16*(2). Retrieved from <http://dx.doi.org/10.1029/2023MS003861> doi: 10.1029/2023ms003861
- Henneman, H. E., & Stefan, H. G. (1999, April). Albedo models for snow and ice on a freshwater lake. *Cold Regions Science and Technology*, *29*(1), 31–48. Retrieved from [http://dx.doi.org/10.1016/S0165-232X\(99\)00002-6](http://dx.doi.org/10.1016/S0165-232X(99)00002-6) doi: 10.1016/s0165-232x(99)00002-6
- Hill, D. F., Burakowski, E. A., Crumley, R. L., Keon, J., Hu, J. M., Arendt, A. A., . . . Wolken, G. J. (2019, July). Converting snow depth to snow water equivalent using climatological variables. *The Cryosphere*, *13*(7), 1767–1784. Retrieved from <http://dx.doi.org/10.5194/tc-13-1767-2019> doi: 10.5194/tc-13-1767-2019
- Hinton, G., Srivastava, N., & Swersky, K. (2012). *Lecture 6e: Rmsprop: Divide the gradient by a running average of its recent magnitude*. University of Toronto.
- Huang, Y., Song, Z., Yang, H., Yu, B., Liu, H., Che, T., . . . Xu, J. (2022, January). Snow cover detection in mid-latitude mountainous and polar regions using nighttime light data. *Remote Sensing of Environment*, *268*, 112766. Retrieved from <http://dx.doi.org/10.1016/j.rse.2021.112766> doi: 10.1016/j.rse.2021.112766
- Innes, M. (2018, May). Flux: Elegant machine learning with julia. *Journal of Open Source Software*, *3*(25), 602. Retrieved from <http://dx.doi.org/10.21105/joss.00602> doi: 10.21105/joss.00602
- Jennings, K. S., Winchell, T. S., Livneh, B., & Molotch, N. P. (2018, March). Spatial variation of the rain–snow temperature threshold across the northern hemisphere. *Nature Communications*, *9*(1). Retrieved from <http://dx.doi.org/10.1038/s41467-018-03629-7> doi: 10.1038/s41467-018-03629-7
- Jensen, A. S., Rittger, K., & Raleigh, M. S. (2024, March). Spatio-temporal patterns and trends in modis-retrieved radiative forcing by snow impurities over

- the western us from 2001 to 2022. *Environmental Research: Climate*, 3(2), 025001. Retrieved from <http://dx.doi.org/10.1088/2752-5295/ad285a> doi: 10.1088/2752-5295/ad285a
- Jia, A., Wang, D., Liang, S., Peng, J., & Yu, Y. (2023, February). Improved cloudy-sky snow albedo estimates using passive microwave and viirs data. *ISPRS Journal of Photogrammetry and Remote Sensing*, 196, 340–355. Retrieved from <http://dx.doi.org/10.1016/j.isprsjprs.2023.01.004> doi: 10.1016/j.isprsjprs.2023.01.004
- Jia, J., Zeng, Z., Tian, B., Chen, S., Chen, L., Wang, Y., . . . Ding, M. (2025, March). The construction of 20-year daily surface albedo along panda transect, antarctica. *Journal of Geophysical Research: Atmospheres*, 130(5). Retrieved from <http://dx.doi.org/10.1029/2024JD042863> doi: 10.1029/2024jd042863
- Keuris, L., Hetzenecker, M., Nagler, T., Mölg, N., & Schwaizer, G. (2023, February). An adaptive method for the estimation of snow-covered fraction with error propagation for applications from local to global scales. *Remote Sensing*, 15(5), 1231. Retrieved from <http://dx.doi.org/10.3390/rs15051231> doi: 10.3390/rs15051231
- Kiem, J., Hammerle, A., Montagnani, L., & Wohlfahrt, G. (2024, April). *Future scenarios of albedo and radiative forcing resulting from changes in snow depth in austria*. Copernicus GmbH. Retrieved from <http://dx.doi.org/10.5194/egusphere-2024-881> doi: 10.5194/egusphere-2024-881
- Klein, A. (2003, July). Validation of daily modis snow cover maps of the upper rio grande river basin for the 2000–2001 snow year. *Remote Sensing of Environment*, 86(2), 162–176. Retrieved from [http://dx.doi.org/10.1016/S0034-4257\(03\)00097-X](http://dx.doi.org/10.1016/S0034-4257(03)00097-X) doi: 10.1016/S0034-4257(03)00097-x
- Klein, A. G., & Stroeve, J. (2002). Development and validation of a snow albedo algorithm for the modis instrument. *Annals of Glaciology*, 34, 45–52. Retrieved from <http://dx.doi.org/10.3189/172756402781817662> doi: 10.3189/172756402781817662
- Kondo, J., & Yamazaki, T. (1990, May). A prediction model for snowmelt, snow surface temperature and freezing depth using a heat balance method. *Journal of Applied Meteorology*, 29(5), 375–384. Retrieved from [http://dx.doi.org/10.1175/1520-0450\(1990\)029<0375:APMFSS>2.0.CO;2](http://dx.doi.org/10.1175/1520-0450(1990)029<0375:APMFSS>2.0.CO;2) doi: 10.1175/1520-0450(1990)029<0375:apmfss>2.0.co;2
- Kouki, K., Räisänen, P., Luoju, K., Luomaranta, A., & Riihelä, A. (2022, March). Evaluation of northern hemisphere snow water equivalent in cmip6 models during 1982–2014. *The Cryosphere*, 16(3), 1007–1030. Retrieved from <http://dx.doi.org/10.5194/tc-16-1007-2022> doi: 10.5194/tc-16-1007-2022
- Krajčič, P., Kirnbauer, R., Parajka, J., Schöber, J., & Blöschl, G. (2017, June). The kühtai data set: 25 years of lysimetric, snow pillow, and meteorological measurements. *Water Resources Research*, 53(6), 5158–5165. Retrieved from <http://dx.doi.org/10.1002/2017WR020445> doi: 10.1002/2017wr020445
- Krinner, G., Derksen, C., Essery, R., Flanner, M., Hagemann, S., Clark, M., . . . Zhu, D. (2018, December). Esm-snowmip: assessing snow models and quantifying snow-related climate feedbacks. *Geoscientific Model Development*, 11(12), 5027–5049. Retrieved from <http://dx.doi.org/10.5194/gmd-11-5027-2018> doi: 10.5194/gmd-11-5027-2018
- Lawrence, D. M., Oleson, K. W., Flanner, M. G., Thornton, P. E., Swenson, S. C., Lawrence, P. J., . . . Slater, A. G. (2011, January). Parameterization improvements and functional and structural advances in version 4 of the community land model. *Journal of Advances in Modeling Earth Systems*, 3(1), n/a-n/a. Retrieved from <http://dx.doi.org/10.1029/2011MS00045> doi: 10.1029/2011ms00045
- Lee, W. Y., Gim, H.-J., & Park, S. K. (2023, November). Parameterizations of

- snow cover, snow albedo and snow density in land surface models: A comparative review. *Asia-Pacific Journal of Atmospheric Sciences*, 60(2), 185–210. Retrieved from <http://dx.doi.org/10.1007/s13143-023-00344-2> doi: 10.1007/s13143-023-00344-2
- Lehning, M., Bartelt, P., Brown, B., & Fierz, C. (2002, November). A physical snowpack model for the swiss avalanche warning. *Cold Regions Science and Technology*, 35(3), 169–184. Retrieved from [http://dx.doi.org/10.1016/S0165-232X\(02\)00072-1](http://dx.doi.org/10.1016/S0165-232X(02)00072-1) doi: 10.1016/S0165-232X(02)00072-1
- Lejeune, Y., Dumont, M., Panel, J.-M., Lafaysse, M., Lapalus, P., Le Gac, E., ... Morin, S. (2019, January). 57years (1960–2017) of snow and meteorological observations from a mid-altitude mountain site (col de porte, france, 1325m of altitude). *Earth System Science Data*, 11(1), 71–88. Retrieved from <http://dx.doi.org/10.5194/essd-11-71-2019> doi: 10.5194/essd-11-71-2019
- Li, H., Zhang, G., Wang, C., Liu, Z., Ju, C., & Mamtimin, A. (2023, March). Improving snow albedo parameterization scheme based on remote sensing data. *Atmospheric Research*, 284, 106602. Retrieved from <http://dx.doi.org/10.1016/j.atmosres.2022.106602> doi: 10.1016/j.atmosres.2022.106602
- Lin, T.-S., He, C., Abolafia-Rosenzweig, R., Chen, F., Wang, W., Barlage, M., & Gochis, D. (2025, February). Improved snow albedo evolution in noah-mp land surface model coupled with a physical snowpack radiative transfer scheme. *Journal of Hydrometeorology*, 26(2), 185–200. Retrieved from <http://dx.doi.org/10.1175/JHM-D-24-0082.1> doi: 10.1175/jhm-d-24-0082.1
- Liu, L., Ma, Y., Menenti, M., Su, R., Yao, N., & Ma, W. (2021, September). Improved parameterization of snow albedo in noah coupled with weather research and forecasting: applicability to snow estimates for the tibetan plateau. *Hydrology and Earth System Sciences*, 25(9), 4967–4981. Retrieved from <http://dx.doi.org/10.5194/hess-25-4967-2021> doi: 10.5194/hess-25-4967-2021
- Livneh, B., Deems, J. S., Schneider, D., Barsugli, J. J., & Molotch, N. P. (2014, November). Filling in the gaps: Inferring spatially distributed precipitation from gauge observations over complex terrain. *Water Resources Research*, 50(11), 8589–8610. Retrieved from <http://dx.doi.org/10.1002/2014WR015442> doi: 10.1002/2014wr015442
- Livneh, B., Xia, Y., Mitchell, K. E., Ek, M. B., & Lettenmaier, D. P. (2010, June). Noah lsm snow model diagnostics and enhancements. *Journal of Hydrometeorology*, 11(3), 721–738. Retrieved from <http://dx.doi.org/10.1175/2009JHM1174.1> doi: 10.1175/2009jhm1174.1
- Magnusson, J., Wever, N., Essery, R., Helbig, N., Winstral, A., & Jonas, T. (2015, April). Evaluating snow models with varying process representations for hydrological applications. *Water Resources Research*, 51(4), 2707–2723. Retrieved from <http://dx.doi.org/10.1002/2014WR016498> doi: 10.1002/2014wr016498
- Malik, M. J., van der Velde, R., Vekerdy, Z., & Su, Z. (2014, June). Improving modeled snow albedo estimates during the spring melt season. *Journal of Geophysical Research: Atmospheres*, 119(12), 7311–7331. Retrieved from <http://dx.doi.org/10.1002/2013JD021344> doi: 10.1002/2013jd021344
- Marks, D. G. (1988). *Climate, energy exchange, and snowmelt in emerald lake watershed, sierra nevada*. Department of Geography and Mechanical Engineering., University of California, Santa Barbara.
- Marshall, S. E. (1989). A physical parameterization of snow albedo for use in climate models, ncar cooperative thesis 123. *Ph. D. Thesis*.
- Menard, C. B., Essery, R., Krinner, G., Arduini, G., Bartlett, P., Boone, A., ... Yuan, H. (2021, January). Scientific and human errors in a snow model intercomparison. *Bulletin of the American Meteorological Society*, 102(1),

- E61–E79. Retrieved from <http://dx.doi.org/10.1175/BAMS-D-19-0329.1>
doi: 10.1175/bams-d-19-0329.1
- Meyer, J. D. D., Jin, J., & Wang, S.-Y. (2012, December). Systematic patterns of the inconsistency between snow water equivalent and accumulated precipitation as reported by the snowpack telemetry network. *Journal of Hydrometeorology*, *13*(6), 1970–1976. Retrieved from <http://dx.doi.org/10.1175/JHM-D-12-066.1> doi: 10.1175/jhm-d-12-066.1
- Molnar, C. (2025). *Interpretable machine learning* (3rd ed.). Author. Retrieved from <https://christophm.github.io/interpretable-ml-book>
- Molotch, N. P., & Bales, R. C. (2006, May). Comparison of ground-based and airborne snow surface albedo parameterizations in an alpine watershed: Impact on snowpack mass balance. *Water Resources Research*, *42*(5). Retrieved from <http://dx.doi.org/10.1029/2005WR004522> doi: 10.1029/2005wr004522
- Mölders, N., Luijting, H., & Sassen, K. (2007, October). Use of atmospheric radiation measurement program data from barrow, alaska, for evaluation and development of snow-albedo parameterizations. *Meteorology and Atmospheric Physics*, *99*(3–4), 199–219. Retrieved from <http://dx.doi.org/10.1007/s00703-007-0271-6> doi: 10.1007/s00703-007-0271-6
- National Research Council. (1999). Making climate forecasts matter. In P. C. Stern & W. E. Easterling (Eds.), (p. 18-37). Washington, DC: The National Academies Press. Retrieved from <https://nap.nationalacademies.org/catalog/6370/making-climate-forecasts-matter> doi: 10.17226/6370
- Nguyen, H., Mehrotra, R., & Sharma, A. (2016). Correcting for systematic biases in gcm simulations in the frequency domain. *Journal of Hydrology*, *538*, 117-126. Retrieved from <https://www.sciencedirect.com/science/article/pii/S0022169416301998> doi: <https://doi.org/10.1016/j.jhydrol.2016.04.018>
- Oaida, C. M., Xue, Y., Flanner, M. G., Skiles, S. M., De Sales, F., & Painter, T. H. (2015, April). Improving snow albedo processes in wrf/ssib regional climate model to assess impact of dust and black carbon in snow on surface energy balance and hydrology over western u.s. *Journal of Geophysical Research: Atmospheres*, *120*(8), 3228–3248. Retrieved from <http://dx.doi.org/10.1002/2014JD022444> doi: 10.1002/2014jd022444
- Oerlemans, J., & Knap, W. H. (1998). A 1 year record of global radiation and albedo in the ablation zone of morteratschgletscher, switzerland. *Journal of Glaciology*, *44*(147), 231–238. Retrieved from <http://dx.doi.org/10.3189/S0022143000002574> doi: 10.3189/s0022143000002574
- O'Neill, A., & Gray, D. M. (1972). Solar radiation penetration through snow. In *The role of snow and ice in hydrology, proceedings of the banff symposium, int. assoc. hydrol. sci* (Vol. 107, pp. 227–240).
- Painter, T. H., Berisford, D. F., Boardman, J. W., Bormann, K. J., Deems, J. S., Gehrke, F., . . . Winstral, A. (2016, October). The airborne snow observatory: Fusion of scanning lidar, imaging spectrometer, and physically-based modeling for mapping snow water equivalent and snow albedo. *Remote Sensing of Environment*, *184*, 139–152. Retrieved from <http://dx.doi.org/10.1016/j.rse.2016.06.018> doi: 10.1016/j.rse.2016.06.018
- Painter, T. H., Bryant, A. C., & Skiles, S. M. (2012, September). Radiative forcing by light absorbing impurities in snow from modis surface reflectance data. *Geophysical Research Letters*, *39*(17). Retrieved from <http://dx.doi.org/10.1029/2012GL052457> doi: 10.1029/2012gl052457
- Painter, T. H., Rittger, K., McKenzie, C., Slaughter, P., Davis, R. E., & Dozier, J. (2009, April). Retrieval of subpixel snow covered area, grain size, and albedo from modis. *Remote Sensing of Environment*, *113*(4), 868–879. Retrieved from <http://dx.doi.org/10.1016/j.rse.2009.01.001> doi: 10.1016/j.rse.2009.01.001
- Palomaki, R. T., Rittger, K., Lenard, S. J., Bair, E., Dozier, J., Skiles, S. M.,

- & Painter, T. H. (2025, August). Assessment of methods for mapping snow albedo from modis. *Remote Sensing of Environment*, 326, 114742. Retrieved from <http://dx.doi.org/10.1016/j.rse.2025.114742> doi: 10.1016/j.rse.2025.114742
- Pike, C., Riley, D., Toal, H., & Burnham, L. (2024, August). Presenting a model to predict changing snow albedo for improving photovoltaic performance simulation. *Solar*, 4(3), 422–439. Retrieved from <http://dx.doi.org/10.3390/solar4030019> doi: 10.3390/solar4030019
- Pirazzini, R., Leppänen, L., Picard, G., Lopez-Moreno, J. I., Marty, C., Macelloni, G., ... Arslan, A. N. (2018, June). European in-situ snow measurements: Practices and purposes. *Sensors*, 18(7), 2016. Retrieved from <http://dx.doi.org/10.3390/s18072016> doi: 10.3390/s18072016
- Qu, X., & Hall, A. (2006). Assessing snow albedo feedback in simulated climate change. *Journal of Climate*, 19(11), 2617 - 2630. Retrieved from <https://journals.ametsoc.org/view/journals/clim/19/11/jcli3750.1.xml> doi: 10.1175/JCLI3750.1
- Rahimi, I., Gandomi, A. H., Chen, F., & Mezura-Montes, E. (2023). A review on constraint handling techniques for population-based algorithms: From single-objective to multi-objective optimization. *Arch. Comput. Methods Eng.*, 30, 2181–2209.
- Raleigh, M. S., Livneh, B., Lapo, K., & Lundquist, J. D. (2015, December). How does availability of meteorological forcing data impact physically based snowpack simulations?*. *Journal of Hydrometeorology*, 17(1), 99–120. Retrieved from <http://dx.doi.org/10.1175/JHM-D-14-0235.1> doi: 10.1175/jhm-d-14-0235.1
- Ranzi, R., & Rosso, R. (1991, 07). A physically based approach to modelling distributed snowmelt in a small alpine catchment. In (Vol. 205, p. 141-150).
- Riley, J. P., Chadwick, D. G., & Eggleston, K. O. (1969). Snowmelt simulation. *Reports, paper 122*.
- Rittger, K., Lenard, S. J. P., Palomaki, R., Brodzik, M., Stillinger, T., Bair, E., ... Painter, T. (2024). *Historical modis/terra l3 global daily 500m sin grid snow cover, snow albedo, and snow physical properties*. National Snow and Ice Data Center. Retrieved from https://nsidc.org/data/STC_MODSCGDRF_HIST/versions/1 doi: 10.7265/F6J3-F387
- Rittger, K., Painter, T. H., & Dozier, J. (2013, January). Assessment of methods for mapping snow cover from modis. *Advances in Water Resources*, 51, 367–380. Retrieved from <http://dx.doi.org/10.1016/j.advwatres.2012.03.002> doi: 10.1016/j.advwatres.2012.03.002
- Rittger, K., Raleigh, M. S., Dozier, J., Hill, A. F., Lutz, J. A., & Painter, T. H. (2020, June). Canopy adjustment and improved cloud detection for remotely sensed snow cover mapping. *Water Resources Research*, 56(6). Retrieved from <http://dx.doi.org/10.1029/2019WR024914> doi: 10.1029/2019wr024914
- Rittger, K., Serreze, M., Brodzik, M. J., Raleigh, M. S., Skiles, M., Musselman, K., ... Team", N. (2023, May). Co-production of snow cover and snow albedo at sub-pixel scale with analysis, uncertainty, and data distribution in near real-time. In *Proceedings of the 2023 modis/viirs science team meeting, panel 8: Snow cover and albedo*. College Park, MD, USA. Retrieved from https://modis.gsfc.nasa.gov/sci_team/meetings/202305/presentations/rittger.pdf (Held 1–4 May 2023 at The Hotel at The University of Maryland. Presentation slides available at: https://modis.gsfc.nasa.gov/sci_team/meetings/202305/presentations/rittger.pdf)
- Roeckner, E., Arpe, K., Bengtsson, L., Brinkop, S., Dümenil, L., Esch, M., ... Windelband, M. (1992). Simulation of the present-day climate with the ecam model: Impact of model physics and resolution. (*:unas*). Retrieved from <https://pure.mpg.de/pubman/item/item.1852612> doi:

- 10.17617/2.1852612
- Rohrer, M. B. (1991). *Die schneedecke im schweizerischen alpenraum und ihre modellierung: Analyse langjähriger schneemessungen und modellierung des wasseräquivalentes aufgrund zeitlich hoch aufgelöster operationell gemessener meteorologischer daten* (Doctoral dissertation, ETH Zurich). doi: 10.3929/ETHZ-A-000601662
- Ryken, A., Bearup, L. A., Jefferson, J. L., Constantine, P., & Maxwell, R. M. (2020, January). Sensitivity and model reduction of simulated snow processes: Contrasting observational and parameter uncertainty to improve prediction. *Advances in Water Resources*, *135*, 103473. Retrieved from <http://dx.doi.org/10.1016/j.advwatres.2019.103473> doi: 10.1016/j.advwatres.2019.103473
- Saito, M., Yang, P., Loeb, N. G., & Kato, S. (2019, May). A novel parameterization of snow albedo based on a two-layer snow model with a mixture of grain habits. *Journal of the Atmospheric Sciences*, *76*(5), 1419–1436. Retrieved from <http://dx.doi.org/10.1175/JAS-D-18-0308.1> doi: 10.1175/jas-d-18-0308.1
- Sarangi, C., Qian, Y., Rittger, K., Bormann, K. J., Liu, Y., Wang, H., ... Painter, T. H. (2019, May). Impact of light-absorbing particles on snow albedo darkening and associated radiative forcing over high-mountain asia: high-resolution wrf-chem modeling and new satellite observations. *Atmospheric Chemistry and Physics*, *19*(10), 7105–7128. Retrieved from <http://dx.doi.org/10.5194/acp-19-7105-2019> doi: 10.5194/acp-19-7105-2019
- Schär, C., Fuhrer, O., Arteaga, A., Ban, N., Charpilloz, C., Di Girolamo, S., ... Wernli, H. (2020, May). Kilometer-scale climate models: Prospects and challenges. *Bulletin of the American Meteorological Society*, *101*(5), E567–E587. Retrieved from <http://dx.doi.org/10.1175/BAMS-D-18-0167.1> doi: 10.1175/bams-d-18-0167.1
- Serreze, M. C., Clark, M. P., Armstrong, R. L., McGinnis, D. A., & Pulwarty, R. S. (1999, July). Characteristics of the western united states snowpack from snowpack telemetry (snotel) data. *Water Resources Research*, *35*(7), 2145–2160. Retrieved from <http://dx.doi.org/10.1029/1999WR900090> doi: 10.1029/1999wr900090
- Shao, D., Xu, W., Li, H., Wang, J., & Hao, X. (2020, September). Modeling snow surface spectral reflectance in a land surface model targeting satellite remote sensing observations. *Remote Sensing*, *12*(18), 3101. Retrieved from <http://dx.doi.org/10.3390/rs12183101> doi: 10.3390/rs12183101
- Shea, J., Wagnon, P., Immerzeel, W., Biron, R., Brun, F., & Pellicciotti, F. (2015, April). A comparative high-altitude meteorological analysis from three catchments in the nepalese himalaya. *International Journal of Water Resources Development*, *31*(2), 174–200. Retrieved from <http://dx.doi.org/10.1080/07900627.2015.1020417> doi: 10.1080/07900627.2015.1020417
- Stigter, E. E., Steiner, J. F., Koch, I., Saloranta, T. M., Kirkham, J. D., & Immerzeel, W. W. (2021, March). Energy and mass balance dynamics of the seasonal snowpack at two high-altitude sites in the himalaya. *Cold Regions Science and Technology*, *183*, 103233. Retrieved from <http://dx.doi.org/10.1016/j.coldregions.2021.103233> doi: 10.1016/j.coldregions.2021.103233
- Stillinger, T., Rittger, K., Raleigh, M. S., Michell, A., Davis, R. E., & Bair, E. H. (2023, February). Landsat, modis, and viirs snow cover mapping algorithm performance as validated by airborne lidar datasets. *The Cryosphere*, *17*(2), 567–590. Retrieved from <http://dx.doi.org/10.5194/tc-17-567-2023> doi: 10.5194/tc-17-567-2023
- Strasser, U., & Marke, T. (2010, November). Escimo.spread – a spreadsheet-based point snow surface energy balance model to calculate hourly snow water equivalent and melt rates for historical and changing climate conditions. *Geoscientific Model Development*, *3*(2), 643–652. Retrieved from <http://dx.doi.org/>

- 10.5194/gmd-3-643-2010 doi: 10.5194/gmd-3-643-2010
- Ström, J., Svensson, J., Honkanen, H., Asmi, E., Dkhar, N. B., Tayal, S., ...
 Hyvärinen, A. (2022). Snow albedo and its sensitivity to changes in deposited light-absorbing particles estimated from ambient temperature and snow depth observations at a high-altitude site in the himalaya. *Elementa: Science of the Anthropocene*, 10(1). Retrieved from <http://dx.doi.org/10.1525/elementa.2021.00118> doi: 10.1525/elementa.2021.00118
- Thackeray, C. W., Qu, X., & Hall, A. (2018). Why do models produce spread in snow albedo feedback? *Geophysical Research Letters*, 45(12), 6223–6231. Retrieved from <https://agupubs.onlinelibrary.wiley.com/doi/abs/10.1029/2018GL078493> doi: <https://doi.org/10.1029/2018GL078493>
- USDA. (2010). Title 210-national engineering handbook, part 622-snow survey and water supply forecasting. In (p. 2-2 - 2-12). Washington, D.C.: Author.
- Verseghy, D. L. (1991, March). Class—a canadian land surface scheme for gcms. i. soil model. *International Journal of Climatology*, 11(2), 111–133. Retrieved from <http://dx.doi.org/10.1002/joc.3370110202> doi: 10.1002/joc.3370110202
- Voordendag, A., Réveillet, M., MacDonell, S., & Lhermitte, S. (2021, September). Snow model comparison to simulate snow depth evolution and sublimation at point scale in the semi-arid andes of chile. *The Cryosphere*, 15(9), 4241–4259. Retrieved from <http://dx.doi.org/10.5194/tc-15-4241-2021> doi: 10.5194/tc-15-4241-2021
- Wang, W., Yang, K., Zhao, L., Zheng, Z., Lu, H., Mamtimin, A., ... Moore, J. C. (2020, April). Characterizing surface albedo of shallow fresh snow and its importance for snow ablation on the interior of the tibetan plateau. *Journal of Hydrometeorology*, 21(4), 815–827. Retrieved from <http://dx.doi.org/10.1175/JHM-D-19-0193.1> doi: 10.1175/jhm-d-19-0193.1
- Wang, Z., Schaaf, C. B., Chopping, M. J., Strahler, A. H., Wang, J., Román, M. O., ... Shuai, Y. (2012, February). Evaluation of moderate-resolution imaging spectroradiometer (modis) snow albedo product (mcd43a) over tundra. *Remote Sensing of Environment*, 117, 264–280. Retrieved from <http://dx.doi.org/10.1016/j.rse.2011.10.002> doi: 10.1016/j.rse.2011.10.002
- Warren, S. G. (1982, February). Optical properties of snow. *Reviews of Geophysics*, 20(1), 67–89. Retrieved from <http://dx.doi.org/10.1029/RG020i001p00067> doi: 10.1029/rg020i001p00067
- Warscher, M., Marke, T., Rottler, E., & Strasser, U. (2024, August). Operational and experimental snow observation systems in the upper rofental: data from 2017 to 2023. *Earth System Science Data*, 16(8), 3579–3599. Retrieved from <http://dx.doi.org/10.5194/essd-16-3579-2024> doi: 10.5194/essd-16-3579-2024
- Wilcoxon, F. (1945, December). Individual comparisons by ranking methods. *Biometrics Bulletin*, 1(6), 80. Retrieved from <http://dx.doi.org/10.2307/3001968> doi: 10.2307/3001968
- Williamson, S. N., Copland, L., & Hik, D. S. (2016, September). The accuracy of satellite-derived albedo for northern alpine and glaciated land covers. *Polar Science*, 10(3), 262–269. Retrieved from <http://dx.doi.org/10.1016/j.polar.2016.06.006> doi: 10.1016/j.polar.2016.06.006
- Wiscombe, W. J., & Warren, S. G. (1980, December). A model for the spectral albedo of snow. i: Pure snow. *Journal of the Atmospheric Sciences*, 37(12), 2712–2733. Retrieved from [http://dx.doi.org/10.1175/1520-0469\(1980\)037<2712:AMFTSA>2.0.CO;2](http://dx.doi.org/10.1175/1520-0469(1980)037<2712:AMFTSA>2.0.CO;2) doi: 10.1175/1520-0469(1980)037<2712:amftsa>2.0.co;2
- Xie, Y., Petterson, C., Flanner, M., & Shates, J. (2024, August). Ground-observed snow albedo changes during rain-on-snow events in northern alaska. *Journal of Geophysical Research: Atmospheres*, 129(16). Retrieved from <http://dx.doi.org/10.1029/2024JD040000> doi: 10.1029/2024JD040000

- .org/10.1029/2024JD040975 doi: 10.1029/2024jd040975
- Yan, H., Sun, N., Wigmosta, M., Skaggs, R., Hou, Z., & Leung, R. (2018, February). Next-generation intensity-duration-frequency curves for hydrologic design in snow-dominated environments. *Water Resources Research*, *54*(2), 1093–1108. Retrieved from <http://dx.doi.org/10.1002/2017WR021290> doi: 10.1002/2017wr021290
- Ye, F., Cheng, Q., Hao, W., Yu, D., Ma, C., Liang, D., & Shen, H. (2023, November). Reconstructing daily snow and ice albedo series for greenland by coupling spatiotemporal and physics-informed models. *International Journal of Applied Earth Observation and Geoinformation*, *124*, 103519. Retrieved from <http://dx.doi.org/10.1016/j.jag.2023.103519> doi: 10.1016/j.jag.2023.103519
- Zhang, Y., & Ohata, T. (2003). Parameterization of albedo on snow/ice surface. a review. *Journal of the Japanese Society of Snow and Ice*, *65*(1), 33–51. Retrieved from <http://dx.doi.org/10.5331/seppyo.65.33> doi: 10.5331/seppyo.65.33
- Zhao, Z., Ding, Y., Wang, M., & Qu, Y. (2025). A radiative transfer model-driven machine learning approach to estimate the snow surface albedo over the greenland ice sheet. *IEEE Transactions on Geoscience and Remote Sensing*, *63*, 1–18. Retrieved from <http://dx.doi.org/10.1109/TGRS.2025.3551094> doi: 10.1109/tgrs.2025.3551094
- Zhongyuan, B., & Ohata, T. (1989, November). Changes in reflectance of glacier no. 1 at the source of the urumqi river in the tianshan mountains during the summer ablation period. *J. Glaciol. Geocryol.*, *11*(4), 311-324.
- Zwart, C., & Fierz, C. (2007). Significance of new snow properties for snow-cover development. In *Geophysical research abstracts* (Vol. 9, p. 10287).